Journal of Computational Physics 464 (2022) 111172

Contents lists available at ScienceDirect

Journal of Computational Physics

www.elsevier.com/locate/jcp

An arbitrary Lagrangian-Eulerian SPH-MLS method for the computation of compressible viscous flows

Luis Ramírez *, Antonio Eirís, Iván Couceiro, José París, Xesús Nogueira

Group of Numerical Methods in Engineering, Universidade da Coruña, Campus de Elviña, 15071, A Coruña, Spain

ARTICLE INFO

Article history:
Received 19 May 2021
Received in revised form 21 March 2022
Accepted 24 March 2022
Available online 28 March 2022

Keywords:
Navier-Stokes equations
Moving Least Squares
Meshless methods
Compressible viscous flows
Smoothed Particle Hydrodynamics

ABSTRACT

In this work we present a high-accurate discretization to solve the compressible Navier-Stokes equations using an Arbitrary Lagrangian-Eulerian meshless method (SPH-MLS), which can be seen as a general formulation that includes some well-known meshfree methods as a particular case. The formulation is based on the use of Moving Least Squares (MLS) approximants as weight functions on a Galerkin formulation and to accurate discretize the convective and viscous fluxes. This formulation also verifies the discrete partition of unity and reproduces the zero-gradient condition for constant functions. Convective fluxes are discretized using Riemann solvers. In order to obtain high accuracy MLS is also used for the high-order reconstruction of the Riemann states.

The accuracy and performance of the proposed method is demonstrated by solving different steady and unsteady benchmark problems.

1. Introduction

Traditionally, grid-based methods have been the most common approach to deal with aerodynamic flows. However, mesh generation is one of the current most significant bottlenecks in CFD applications, since it is usual that the mesh generation phase represents the dominant cost in terms of both, human intervention and time. Moreover, there are problems with moving boundaries that complicates the meshing and remeshing algorithm. Meshless methods are a potential choice to solve problems such as free surface flows, sloshing, floods and fluid-structure interaction, among others, where mesh-based methods are difficult to apply. In the context of CFD, the Smoothed Particle Hydrodynamics method (SPH) is the most widely used meshless method for flow simulations. Unfortunately, this method currently presents some key drawbacks, which have been a serious barrier to its widespread use [1]. The lack of accuracy, low convergence order and inaccurate definition of boundary conditions are the kinds of drawbacks that a new generation of meshless methods have to overcome.

Meshless and mesh-based discretizations are usually considered as two competitive strategies to solve partial differential equations. In fact, if we consider the Finite Volume Method (FVM) and Smoothed Particle Hydrodynamics (SPH) as representative of these two approaches, both methodologies are far apart from each other. Vila [2] linked these methodologies by devising a weak version of a SPH method in an ALE framework where the interaction between particles is accounted by solving a Riemann problem. Junk [4] outlined that the FVM can be considered as a special case of meshless method satisfying the partition of unity property and posed the question if finite volume method really needs a topology for its

* Corresponding author.
E-mail address: luis.ramirez@udc.es (L. Ramírez).

https://doi.org/10.1016/j.jcp.2022.111172

implementation. Schaller [5] analyzed three particle methods in decreasing similitude with the FVM and in terms of computational cost. The particle method with more similitude with the FVM is the one based on Voronoi tessellation, followed by the FVPM [6] and the SPH-ALE proposed by Vila [2] and Ben Moussa [3]. So, this two apparent different approaches actually have many features in common [7] suggesting that some successful techniques used in FVM can be incorporated in SPH and viceversa.

Despite the fact that meshless and mesh-based methods have advantages and drawbacks derived from the different form to accomplish the discretization of the partial differential equations, there are some physical phenomena (like turbulence) that are very computational demanding for both types of approaches. The research on the numerical simulation of turbulent flows has been mainly addressed by using mesh-based methods. Simulation of turbulence using meshfree methods has received less attention, and many studies deal with complex applications without providing details of their development, diffusion rates or details about the evolution of the energy spectrum. We refer the reader to [8–12] for some examples.

In [13] the authors presented a new meshless approach (SPH-MLS) based on a Galerkin discretization of a set of conservation equations on an Arbitrary Lagrangian Eulerian approach, applied to the resolution of the Linearized Euler Equations. Instead of using kernel approximations, Moving Least Squares (MLS) [14,15] were used as weight functions for the Galerkin discretization. The numerical method proposed was high-order and very accurate, and it was shown that it was able to be applied in the context of Computational Aeroacoustics. It can be seen as a general formulation which includes some well-known meshfree methods as a particular case, such as SPH-ALE [2,16–18] and Finite Point Method [19–21]. This formulation has several advantages over standard SPH methods. First, MLS functions form a partition of unity even in regions close to the boundaries. Moreover, shape function derivatives form a partition of nullity. These properties allow avoiding problems related with the initial position of particles which are found in other SPH methods [22] and also lead to a higher accuracy than kernel usual approximations. Moreover, the number of neighbors required by the proposed formulation is smaller than that required when the kernel approximation is used [13], so the numerical scheme is more compact. In addition, the ALE behavior of the method proposed in this work makes possible the natural accommodation of Particle Shifting Techniques (PST). PST defines a drift velocity that moves the computational points to positions that produce more regular distributions and thus more accurate results [23]. First attempts to use MLS under a meshless framework are the Diffuse Element Method [24] and the Element-Free Galerkin [25]. Dilts [26,27] proposed different procedures to introduce MLS approximations to derive discrete meshless methods applied to a system of equations expressed in Lagrangian form. We note that the novelty of the present work is the use of the MLS approximation technique in a weak form of the Navier Stokes equations in ALE form.

In this work, we present several modifications to the method proposed in [13] and also the extension of this method to the resolution of compressible viscous flows in both laminar and turbulent regimes. Thus, there are two main novelties in the formulation. First, we introduce a novel approach for the high-order reconstruction of the Riemann states. The usual Taylor polynomial reconstruction of the Riemann states is substituted by direct MLS approximations. This avoids the need of computing high-order derivatives for the Taylor reconstruction, but at the same time keeps the high-order accuracy of the reconstruction. The second novelty is related to the discretization of viscous terms. In the literature, there are different approaches to model the viscous part of the Navier-Stokes equations [28–31]. The traditional approach in SPH methods is based on the definition of a number of discrete operators for approximating second derivatives. In this work we follow a different approach and approximate the viscous flux term with a formulation similar to that used for mesh-based methods in unstructured grids. Our approach is based on the use of MLS approximations of the Riemann states at both sides of the integration point. This approach fits perfectly in the SPH-MLS approach, since the MLS reconstruction is already computed. This new discretization leads to a robust and very accurate meshless method, which is able to obtain results at least as accurate as grid-based methods of the same order of accuracy.

The structure of this paper is as follows: firstly the governing equations are presented. Next, the proposed numerical method is introduced, including the novel discretization of viscous terms. Some numerical examples are presented to show the accuracy and robustness of the proposed formulation. Finally, conclusions are drawn.

2. Governing equations

We define a transport operator $L_{\boldsymbol{w}}(\boldsymbol{U})$ with a velocity field $\boldsymbol{w}$ that operates on a vector of variables $\boldsymbol{U}$ giving

$$L_{\boldsymbol{w}}(\boldsymbol{U}) \equiv \frac{\partial}{\partial t}\boldsymbol{U} + \nabla \cdot (\boldsymbol{w} \otimes \boldsymbol{U}) \tag{1}$$

The conservative form of the Navier-Stokes equations can be compactly expressed using the transport operator $L_{\boldsymbol{w}}$ as

$$L_{\boldsymbol{w}}(\boldsymbol{U}) + \nabla \cdot (\boldsymbol{F}_H - \boldsymbol{F}_E) = \boldsymbol{S} \tag{2}$$

where the fluxes are split into a hyperbolic-like part, $\boldsymbol{F}_H = (\boldsymbol{F}_H^x, \boldsymbol{F}_H^y, \boldsymbol{F}_H^z)$, and an elliptic-like part, $\boldsymbol{F}_E = (\boldsymbol{F}_E^x, \boldsymbol{F}_E^y, \boldsymbol{F}_E^z)$. The right hand side contains the vector of source terms $\boldsymbol{S}$.

In 3D the vector of conservative variables reads as

$$\boldsymbol{U} = \begin{pmatrix} \rho \\ \rho u^x \\ \rho u^y \\ \rho u^z \\ \rho E \end{pmatrix}, \tag{3}$$

where ρ is the density, $\boldsymbol{u} = (u^x, u^y, u^z)^T$ is the velocity vector, and E is the total energy.

The hyperbolic-like fluxes, also known as convective fluxes read in 3D as

$$\boldsymbol{F}_H^x = \begin{pmatrix} \rho(u^x - w^x) \\ \rho u^x(u^x - w^x) + p \\ \rho u^y(u^x - w^x) \\ \rho u^z(u^x - w^x) \\ \rho E(u^x - w^x) + p u^x \end{pmatrix}, \quad \boldsymbol{F}_H^y = \begin{pmatrix} \rho(u^y - w^y) \\ \rho u^x(u^y - w^y) \\ \rho u^y(u^y - w^y) + p \\ \rho u^z(u^y - w^y) \\ \rho E(u^y - w^y) + p u^y \end{pmatrix},$$
$$\boldsymbol{F}_H^z = \begin{pmatrix} \rho(u^z - w^z) \\ \rho u^x(u^z - w^z) \\ \rho u^y(u^z - w^z) \\ \rho u^z(u^z - w^z) + p \\ \rho E(u^z - w^z) + p u^z \end{pmatrix} \tag{4}$$

where p is the pressure. The elliptic or viscous fluxes read

$$\boldsymbol{F}_E^x = \begin{pmatrix} 0 \\ \tau^{xx} \\ \tau^{xy} \\ \tau^{xz} \\ \boldsymbol{\tau}^x \cdot \boldsymbol{u} - q^x \end{pmatrix}, \quad \boldsymbol{F}_E^y = \begin{pmatrix} 0 \\ \tau^{yx} \\ \tau^{yy} \\ \tau^{yz} \\ \boldsymbol{\tau}^y \cdot \boldsymbol{u} - q^y \end{pmatrix}, \quad \boldsymbol{F}_E^z = \begin{pmatrix} 0 \\ \tau^{zx} \\ \tau^{zy} \\ \tau^{zz} \\ \boldsymbol{\tau}^z \cdot \boldsymbol{u} - q^z \end{pmatrix}, \tag{5}$$

where $\boldsymbol{\tau}^x = (\tau^{xx}, \tau^{xy}, \tau^{xz})$, $\boldsymbol{\tau}^y = (\tau^{yx}, \tau^{yy}, \tau^{yz})$ and $\boldsymbol{\tau}^z = (\tau^{zx}, \tau^{zy}, \tau^{zz})$ represent the viscous stresses and $\boldsymbol{q} = (q^x, q^y, q^z)^T$ is the heat flux vector.

The viscous stress tensor is defined as

$$\boldsymbol{\tau} = \mu(\nabla(\boldsymbol{u}) + \nabla(\boldsymbol{u})^T) - \frac{2}{3}\mu\nabla \cdot (\boldsymbol{u})\boldsymbol{I}$$

where μ is the dynamic viscosity. These equations are completed with an equation of state (EOS), which in this work is the ideal gas EOS, defined as

$$\boldsymbol{p} = (\gamma - 1)\left(\rho E - \frac{1}{2}\rho\,|\boldsymbol{u}|^2\right), \tag{6}$$

where $\gamma = \frac{7}{5}$.

Once the governing equations have been presented we can remark some details. The hyperbolic flux $\boldsymbol{F}_H$ is not only dependent on the vector of conservative variables $\boldsymbol{U}$ but also on the transport velocity field $\boldsymbol{w}$, stated mathematically as $\boldsymbol{F}_H = \boldsymbol{F}_H(\boldsymbol{U}, \boldsymbol{w})$. The elliptic flux $\boldsymbol{F}_E$ is a diffusive flux that does not depend on $\boldsymbol{w}$ velocity and it takes the form $\boldsymbol{F}_E = \boldsymbol{F}_E(\boldsymbol{U}, \nabla(\boldsymbol{u}))$. Note that the case $\boldsymbol{w} = \boldsymbol{0}$ corresponds to the usual Eulerian approach. By setting the transport field equal to the fluid velocity field $\boldsymbol{w} = \boldsymbol{u}$ leads to a pure Lagrangian approach. But apart from these two extreme cases, where the transport velocity is zero or equal to the fluid velocity in the whole domain, there are other possible scenarios. The transport velocity is a field variable that is independent of the flow solution and can be prescribed at different points of the domain according to different criteria. The transport velocity can be prescribed to move particles avoiding some pitfalls of pure Lagrangian methods by using some Particle Shifting Technique [23]. Particles in the vicinity of a free surface can be moved in a Lagrangian fashion meanwhile particles in the vicinity of a wall can adopt an Eulerian framework to ease the implementation of boundary conditions. Note that the present framework allows both Eulerian and Lagrangian frames for each particle, since it is an Arbitrary Lagrangian-Eulerian (ALE) approach.

3. Numerical discretization

In this section the numerical discretization of the system of equations (2) is presented. The first step in the discretization process is the reduction of the continuum domain into a cloud of points. Fig. 1 shows a discretized geometry corresponding to a continuous domain Ω with boundary $\partial\Omega$.

The points also serve as the location of the computational nodes or computational particles. Node is the preferred option to refer to computational points in Eulerian description meanwhile particle is the preferred one in Lagrangian description.

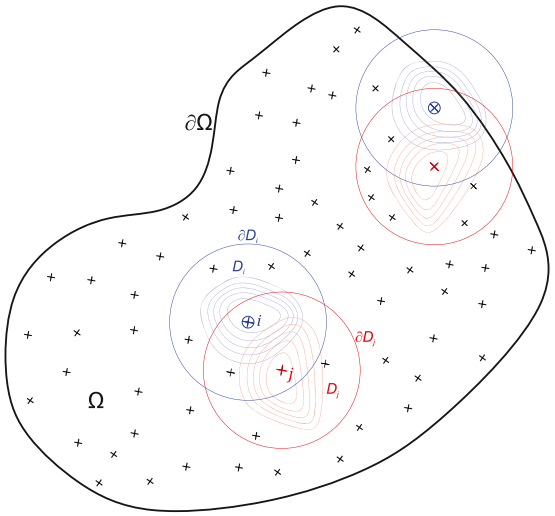

Fig. 1. Computational domain Ω and kernel support D_i and D_j of particle i and j. Shape functions associated to particle i and j are represented by isocontour curves.

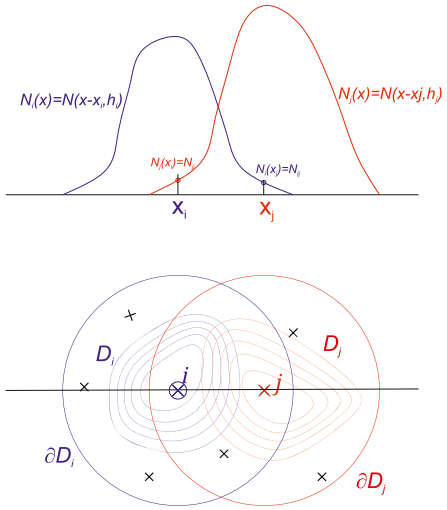

Fig. 2. Shape functions associated to particle i and j are represented by isocontour curves.

In ALE methods the computational points can be fixed nodes, particles that move with the fluid velocity or some points that move with a different prescribed transport velocity $\boldsymbol{w}$. Instead of using different names we use the term particle in broad sense to refer to any computational point. We denote by n the total numbers of particles.

Each particle is labeled with an index i and we define its current position by means of its vector position $\boldsymbol{x}_i$ with respect to a fixed coordinate system. We denote by D_i the spherical support domain and by N_i the shape function associated to particle i. We use lowercase n_i for the number of particles inside the support domain of i particle. Note that each shape function N_i has a spherical compact support (a circle for 2D) but, in general, the shape function is not a centered radial function. Fig. 2 depicts two neighboring particles in a two-dimensional domain. The bottom of the figure corresponds to a plan view meanwhile the top view shows the profile of the shape functions in a normal plane passing through the line that connects both particles. Note that we show the continuous version of the shape functions $N_i(x)$ and $N_j(x)$ although only the values in the locations of particles are required ($N_i(x_j)$ and $N_j(x_i)$).

Contrary to traditional SPH methods, where each particle is assigned with a constant mass value, in the proposed method the mass and volume for each particle are variables that evolve with time.

The complete procedure to obtain the discretization can be found in [13] for a general system of conservation laws. Here, we start with the following semidiscrete form valid for any interior particle i whose support does not intersect $\partial\Omega$ (see Fig. 1), where we group the hyperbolic and elliptic fluxes in a total flux represented by $\mathcal{F}$ in order to remark the general form of a balance law.

$$\frac{d(V_i \boldsymbol{U}_i)}{dt} + \sum_{j=1}^{n_i} \left[\frac{1}{2} \left(\boldsymbol{\mathcal{F}}_j + \boldsymbol{\mathcal{F}}_i \right) - \boldsymbol{\mathcal{F}}_i \right] \left(-V_j \nabla N_{ij} + V_i \nabla N_{ji} \right) = V_i \boldsymbol{S}_i \tag{7}$$

The first term in the left side of the equation is the temporal derivative of the quantity carried by a general particle i. For a fixed particle with $\boldsymbol{w}_i = \boldsymbol{0}$ the term $\frac{d(V_i \boldsymbol{U}_i)}{dt}$ is equivalent to $\frac{\partial(V_i \boldsymbol{U}_i)}{\partial t}$. For a particle with $\boldsymbol{w}_i = \boldsymbol{u}_i$ the temporal derivative $\frac{d(V_i \boldsymbol{U}_i)}{dt}$ represents a material derivative which is usually represented as $\frac{D(V_i \boldsymbol{U}_i)}{Dt}$. The second term is a sum over all neighbors of particle i and accounts for the hyperbolic and elliptic fluxes of particle i. We note that the usual kernel approximation has been substituted by a discretization based in MLS approximations.

In equation (7), we define $N_{ij} = N(\boldsymbol{r}_j - \boldsymbol{r}_i, h_i)$ and $N_{ji} = N(\boldsymbol{r}_i - \boldsymbol{r}_j, h_j)$. Note that these terms are required to obtain a anti-symmetric discretization of the effective area of the particle. By comparison with finite volume methods, the term $\left(-V_j \nabla N_{ij} + V_i \nabla N_{ji} \right)$ plays the same role as the geometric interaction area between cells i and j.

The notation $N_i = N(\boldsymbol{r} - \boldsymbol{r}_i, h_i)$ stands for the MLS shape function evaluated at point $\boldsymbol{r}$ and centered at the position of particle i ($\boldsymbol{r}_i$). MLS shape functions also depend on a weighted function (see [32]), and the smoothing length h_i which is a measure of the compact support of the kernel function. The smoothing length associated to the particle i is variable for each particle and is computed as

$$h_i = \sigma V_i^{\frac{1}{d}} \tag{8}$$

where d is the space dimensions number, V_i is the effective volume of the particle i and σ is a constant parameter. The number of neighbors is variable and it depends on the value of σ. In this work, we use $\sigma = 1.5$ in the numerical applications. Note that this value differs from the one typically used in SPH-kernel approaches ($\sigma = 2$). This implies that the number of particles involved in the approximation is reduced, which reduces the computational cost and also increases the accuracy of the method.

For the discretization of the Navier-Stokes equations we split the $\boldsymbol{\mathcal{F}}$ flux into the convective and the diffusive parts $\boldsymbol{\mathcal{F}} = \boldsymbol{F}^H - \boldsymbol{F}^E$ and we define the flux at the midpoint between two particles i and j as $\boldsymbol{F}_{ij} = \frac{1}{2} \left(\boldsymbol{F}_j + \boldsymbol{F}_i \right)$. Then, we can write

$$\frac{d(V_i \boldsymbol{U}_i)}{dt} + \sum_{j=1}^{n_i} \left[\boldsymbol{F}_{ij}^H - \boldsymbol{F}_i^H - \left(\boldsymbol{F}_{ij}^E - \boldsymbol{F}_i^E \right) \right] \left(-V_j \nabla N_{ij} + V_i \nabla N_{ji} \right) = V_i \boldsymbol{S}_i \tag{9}$$

Following [13] we introduce the numerical flux for the convective terms as an approximation of the flux at the midpoint between particles $\boldsymbol{G}_{ij} \approx \boldsymbol{F}_{ij}^H$, and we obtain the final discretized form

$$\frac{d(V_i \boldsymbol{U}_i)}{dt} + \sum_{j=1}^{n_i} \left[\boldsymbol{G}_{ij} - \boldsymbol{F}_i^H - \left(\boldsymbol{F}_{ij}^E - \boldsymbol{F}_i^E \right) \right] \left(-V_j \nabla N_{ij} + V_i \nabla N_{ji} \right) = V_i \boldsymbol{S}_i \tag{10}$$

Moving Least Squares approximations are used also to provide high accurate discretization of the convective and diffusive fluxes. We provide a brief exposition to introduce the nomenclature and remark some important points.

3.1. Moving Least Squares approximation

Moving Least Squares is an approximation technique widely used in meshless methods with different purposes. In standard SPH methodology MLS is used as an auxiliary tool for boundary treatment [33], field refreshing to remedy the noisy pressure field [34], reordering SPH methods or simply as an approximation technique in the post-processing stage. In SPH-ALE methods [16,17] MLS technique is used to increase the accuracy of convective fluxes.

In this work, MLS approximations play a more important role, since the usual kernel approximation is totally replaced by the MLS approximation.

First, we give a brief overview of the Moving Least Squares (MLS) technique for introducing the notations. We refer the reader to [14] for a complete description of the technique and to [35] for their application in the context of meshless methods.

The MLS approximation of a function u at point $\boldsymbol{r} = (x, y, z)^T$ is approximated in the neighborhood around a particle i by a set of n_i values, u_j, and it is defined as

$$\widehat{u}(\boldsymbol{r}) = \sum_{j=1}^{n_i} N_j(\boldsymbol{r}) u_j \tag{11}$$

where the associated shape functions, gathered in vector $\boldsymbol{N} = (N_1, N_2, ..., N_{n_i}) \in \mathbb{R}^{n_i}$, are computed by

$$\boldsymbol{N}^T(\boldsymbol{r}) = \boldsymbol{p}^T(\boldsymbol{r}) \boldsymbol{M}^{-1}(\boldsymbol{r}) \boldsymbol{P}(\boldsymbol{r}) \boldsymbol{W}_{MLS}(\boldsymbol{r}) \tag{12}$$

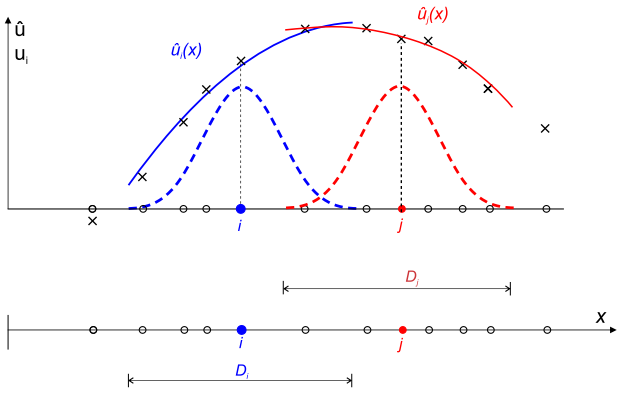

Fig. 3. Schematic representation of MLS approximations. The blue solid line represents the MLS reconstruction associated to particle i, built from information of its neighboring particles. The blue dashed line represents the weight function. The same is plotted in red for another particle j. D_i and D_j are the supports of particles i and j. (For interpretation of the colors in the figure(s), the reader is referred to the web version of this article.)

where $\boldsymbol{p}^T(\boldsymbol{r}) = (1, x, y, z, x^2, y^2, z^2, xy, xz, yz...) \in \mathbb{R}^m$ is a m-dimensional basis functions vector, $\boldsymbol{P}(\boldsymbol{r})$ is a $m \times n_i$ matrix where the basis functions are evaluated at each point of the stencil of the particle i (namely $\boldsymbol{P} = [\boldsymbol{p}^T(\boldsymbol{r_j})]_i$) and $\boldsymbol{M}(\boldsymbol{r})$ is the $m \times m$ moment matrix given by

$$\boldsymbol{M}(\boldsymbol{r}) = \boldsymbol{P}(\boldsymbol{r})\boldsymbol{W}_{MLS}(\boldsymbol{r})\boldsymbol{P}^T(\boldsymbol{r}). \tag{13}$$

Diagonal matrix $\boldsymbol{W}_{MLS}(\boldsymbol{r})$ is derived from the kernel function evaluated at $\boldsymbol{r}_j - \boldsymbol{r}_i$ for the n_i neighboring particles [36].

Note that the general MLS technique allows that $\boldsymbol{r}$ can take any value in the domain Ω resulting in a continuous approximation. Therefore, the approximation of the variables or its derivatives can be obtained at any point of the domain. In Fig. 3 a schematic representation of the MLS reconstruction is shown.

In the following sections we address the discretization of the convective and diffusive fluxes.

3.2. Convective flux discretization

In this work we have computed the convective flux, $\boldsymbol{G}_{ij}$, using the Rusanov numerical flux [37].

$$\boldsymbol{G}_{ij} = \frac{1}{2}(\boldsymbol{F}_{ij}^{+} + \boldsymbol{F}_{ij}^{-}) - \frac{1}{2}S_{ij}^{*}\Delta\boldsymbol{U}_{ij} \cdot \boldsymbol{n}, \tag{14}$$

where S_{ij}^{*} is the maximum eigenvalue of the Jacobian matrix

$$S_{ij}^{*} = \max\left((\boldsymbol{u} - \boldsymbol{w}) \cdot \boldsymbol{n} + c_{ij}, (\boldsymbol{u} - \boldsymbol{w}) \cdot \boldsymbol{n} - c_{ij}, (\boldsymbol{u} - \boldsymbol{w}) \cdot \boldsymbol{n}\right). \tag{15}$$

In (15), c_{ij} is the local speed of sound at the integration point and $\boldsymbol{F}_{ij}^{-}$ and $\boldsymbol{F}_{ij}^{+}$ denote the flux approximations of $\boldsymbol{F}$ on the left and right sides of the integration point (the two different Riemann states), and $\boldsymbol{n}_{ij}$ is the normal vector. The jump of the conservative vector is defined as $\Delta\boldsymbol{U}_{ij} = \hat{\boldsymbol{U}}_{ij}^{+} - \hat{\boldsymbol{U}}_{ij}^{-}$.

In order to achieve a high-order reconstruction of the Riemann states, the usual approach is to use a Taylor polynomial. Instead, we propose here the use of MLS approximations. Note that the MLS shape functions required for the reconstruction are already computed since they are used in the discretization of the governing equations, as indicated in equation (10). Thus, the cost of the evaluation of the reconstructed Riemann states is highly reduced, compared with the use of a Taylor polynomial (which requires an additional computation of high-order derivatives). Thus the reconstructed variables are computed as

$$\hat{\boldsymbol{U}}_{ij}^{-} = \sum_{k=1}^{n_i} N(\boldsymbol{r}_{ij} - \boldsymbol{r}_i, h_i)\boldsymbol{U}_k, \;\; \hat{\boldsymbol{U}}_{ij}^{+} = \sum_{k=1}^{n_j} N(\boldsymbol{r}_{ij} - \boldsymbol{r}_j, h_j)\boldsymbol{U}_k \tag{16}$$

3.3. Diffusive flux discretization

In this work, we use a novel formulation for the discretization of the diffusive fluxes, which is also based on the use of MLS approximations. MLS shape functions allows us to obtain high-accurate reconstructions of the variables on each stencil. Thus, it is possible to obtain two high-order approximations of the diffusive fluxes at the integration point using the two different states, and then compute the diffusive fluxes directly at each integration point (which is located at the midpoint

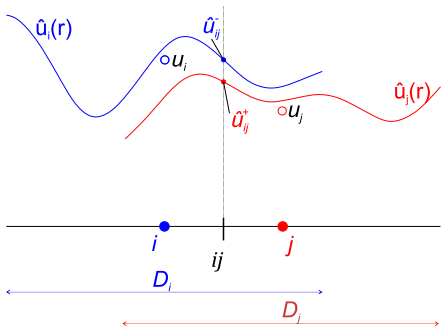

Fig. 4. Schematic representation of the high-order Riemann states reconstruction at the integration point located in the midpoint between particles i and j.

between particles i and j), as the arithmetic mean of the diffusive fluxes of each Riemann state. (See Fig. 4.) A different approach is to center the MLS approximation on each integration point and perform a reconstruction for every integration as it was already proposed in the context of Finite Volume methods [36,38]. However, this approach will lead to higher computational cost due the large number of integration points and the need for computing the reconstructions on each time step. Thus, in this work, the diffusive fluxes are computed as

$$\boldsymbol{F}_{ij}^{E} = \frac{1}{2}(\boldsymbol{F}_{ij}^{E+} + \boldsymbol{F}_{ij}^{E-}). \tag{17}$$

4. Numerical results

This section presents the numerical results for several benchmark problems aimed at assessing the accuracy and efficiency of the proposed method for both steady and unsteady problems. All the numerical examples have been computed using a third-order TVD Runge–Kutta scheme for time integration [39]. This time integration method has been already used in SPH [16].

4.1. Accuracy and convergence test

In this section we test the accuracy and the order of convergence of the proposed reconstruction. First, we have considered the 1D domain $\Omega = [0, 4]$, which is discretized with a set of uniform and random particles. The random particles are obtained adding a perturbation to the position of the uniform distribution. This perturbation is randomly distributed between $[-\frac{V}{2}, \frac{V}{2}]$. where V is the volume associated to each particle of the initial uniform set. Each particle is initialized with the field function $u(x)$ as

$$u(x) = \sin(2\pi x) \tag{18}$$

First, we analyze the accuracy of the MLS reconstruction of the variable at each integration point (midpoint between particles). The reconstruction of the variable and its derivatives are computed as

$$u(x_{ij}) \approx \hat{u}(x_{ij}) = \sum_{k=1}^{n_j} N(\boldsymbol{r}_{ij} - \boldsymbol{r}_i, h_i)\boldsymbol{u}_k \tag{19}$$

$$\frac{\partial u(x_{ij})}{\partial x} \approx \frac{\partial \hat{u}(x_{ij})}{\partial x} = \sum_{k=1}^{n_j} \frac{\partial N(\boldsymbol{r}_{ij} - \boldsymbol{r}_i, h_i)}{\partial x}\boldsymbol{u}_k \tag{20}$$

$$\frac{\partial^2 u(x_{ij})}{\partial x^2} \approx \frac{\partial^2 \hat{u}(x_{ij})}{\partial x^2} = \sum_{k=1}^{n_j} \frac{\partial^2 N(\boldsymbol{r}_{ij} - \boldsymbol{r}_i, h_i)}{\partial x^2}\boldsymbol{u}_k \tag{21}$$

For each distribution of particles, the L_2^N norms of the errors are computed, and the obtained results are presented in Fig. 5.

The expected orders of accuracy are recovered for the approximation of the variable and its derivatives. Note that the choice of $\sigma = 2.0$ leads to a larger error than that of $\sigma = 1.5$ for all the discretizations.

Next, we analyze the convergence and the error committed by the MLS reconstruction centered at each particle (Fig. 6). The centered reconstruction is used in the computation of the weights and the evaluation of the diffusive flux on each particle. The reconstruction is computed as

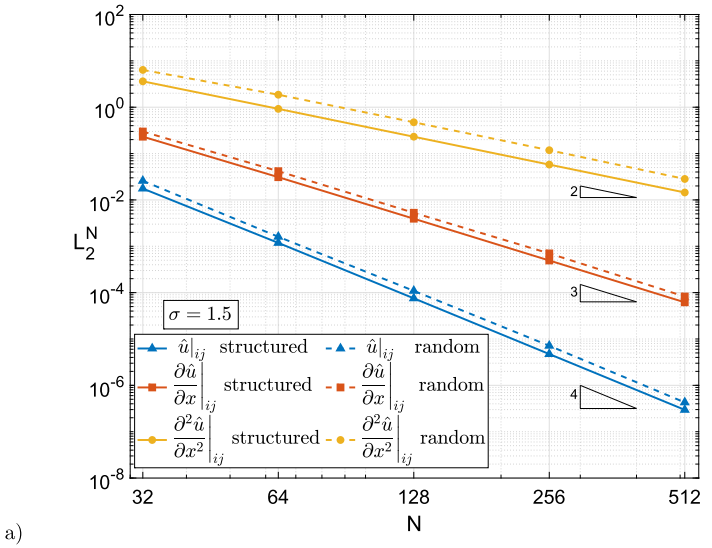

a)

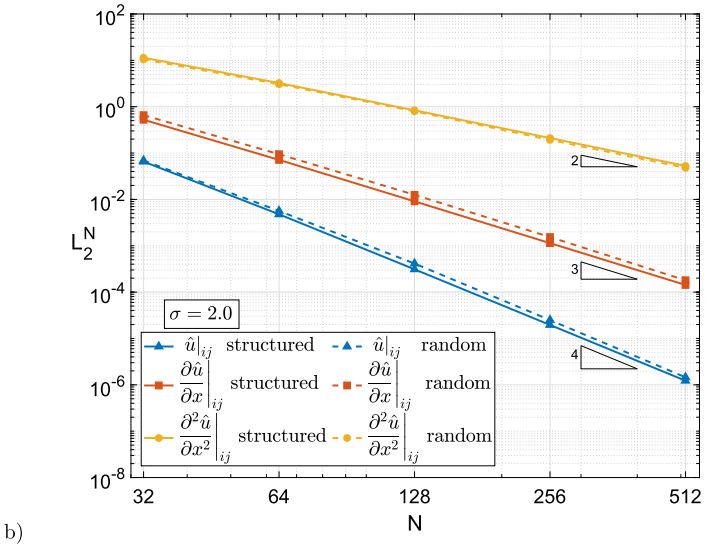

b)

Fig. 5. Accuracy and convergence 1D test: L_2^N norm of the committed error at the approximation of the variables and its derivatives at integrations points (midpoint between neighboring particles) for each discretization. Figure a) shows the obtained results with the parameter $\sigma = 1.5$ and Figure b) those obtained for $\sigma = 2.0$.

$$\frac{\partial u(x_I)}{\partial x} \approx \frac{\partial \hat{u}(x_I)}{\partial x} = \sum_{k=1}^{n_j} \frac{\partial N(\boldsymbol{r}_i - \boldsymbol{r}_i, h_i)}{\partial x} \boldsymbol{u}_k \tag{22}$$

$$\frac{\partial^2 u(x_I)}{\partial x^2} \approx \frac{\partial^2 \hat{u}(x_I)}{\partial x^2} = \sum_{k=1}^{n_j} \frac{\partial^2 N(\boldsymbol{r}_i - \boldsymbol{r}_i, h_i)}{\partial x^2} \boldsymbol{u}_k \tag{23}$$

$$\frac{\partial^3 u(x_I)}{\partial x^3} \approx \frac{\partial^3 \hat{u}(x_I)}{\partial x^3} = \sum_{k=1}^{n_j} \frac{\partial^3 N(\boldsymbol{r}_i - \boldsymbol{r}_i, h_i)}{\partial x^3} \boldsymbol{u}_k \tag{24}$$

The expected order of accuracy is achieved in all cases. Note that when a structured distribution of particles is used, the order of the reconstruction increases in the odd derivatives. This is due to the cancellation of errors when a symmetric discretization is used.

Next, we have tested the effect of the parameter σ. This parameter regulates the size of the support. We have discretized the computational domain $\Omega = [0, 4]$ with 128 particles, with both, uniform and random distributions. Then, we have computed the L_2^N norms of the error for values of $\sigma \in [1, 3]$. The L_2^N norms of the error for the reconstruction and its derivatives at the integration point and the derivatives at the particle position are represented in Fig. 7.

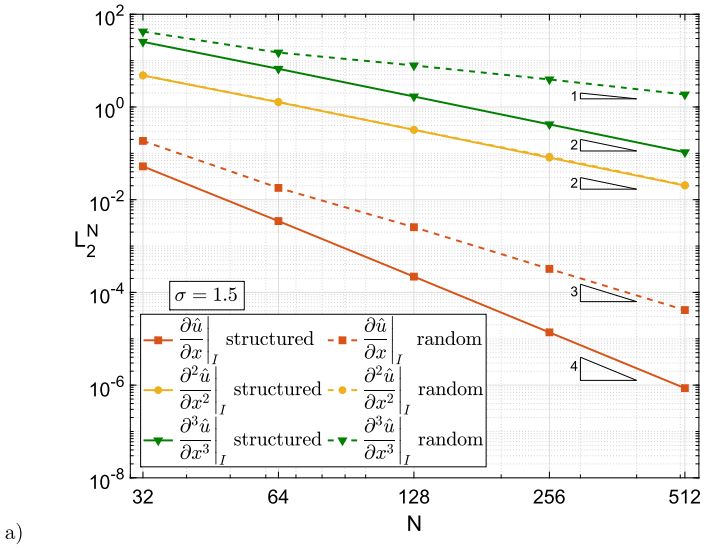

a)

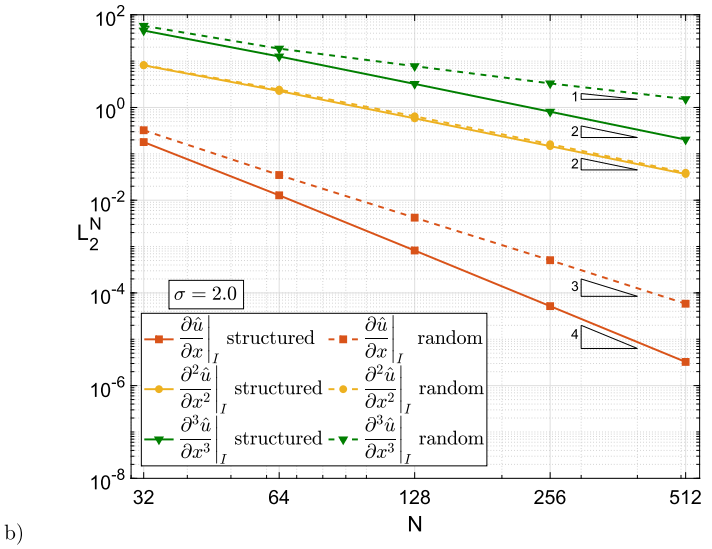

b)

Fig. 6. Accuracy and convergence 1D test: L_2^N norm of the committed error at the approximation of the derivatives at the particles position for each discretization. Figure a) shows the obtained results with the parameter $\sigma = 1.5$ and Figure b) those obtained for $\sigma = 2.0$.

Note that the committed error in the reconstruction decreases as the value of σ decreases. However, when random particle distributions are used, the minimum value of σ that is able to obtain results is $\sigma = 1.37$. Below that value, there are reconstructions in the domain that does not have enough points to use the MLS reconstruction.

For each value of σ, we have calculated the number of neighbors for each particle for uniform distributions and the mean value and maximum and minimum values for random distributions. The obtained results are represented in Fig. 8. For uniform distributions of particles, the typical value used in SPH ($\sigma = 2$) leads to 9 neighbors for each particle, that is, 8 Riemann Problems to be solved each time step. On the other hand, if $\sigma = 1.5$ is chosen, the number of neighbors is reduced to 7, which implies a computation of 6 Riemann Problems. In the case of random distributions, the mean number of neighbors is 7.875 for $\sigma = 2$ and 6.094 for $\sigma = 1.5$. This difference increases in 2D and 3d. For example, on a 2D uniform distribution of particles a value of $\sigma = 1.5$ leads to 25 neighbors per particle and $\sigma = 2.0$ leads to 49 neighbors per particle. In a 3D case a $\sigma = 1.5$ leads to 123 neighbors per particle and $\sigma = 2.0$ leads to 257 neighbors per particle.

From the previous results, we recommend the use of $\sigma = 1.5$ as a compromise between accuracy and robustness.

Next, we have extended the problem to 2D. We have considered the domain $\Omega = [0, 4] \times [0, 4]$, which is discretized with a set of uniform and random particles of 1024, 4096, 16384 and 65536. The field function, $u(x, y)$, analyzed in this test case is defined as

$$u(x, y) = \sin(2\pi x) \sin(2\pi y) \tag{25}$$

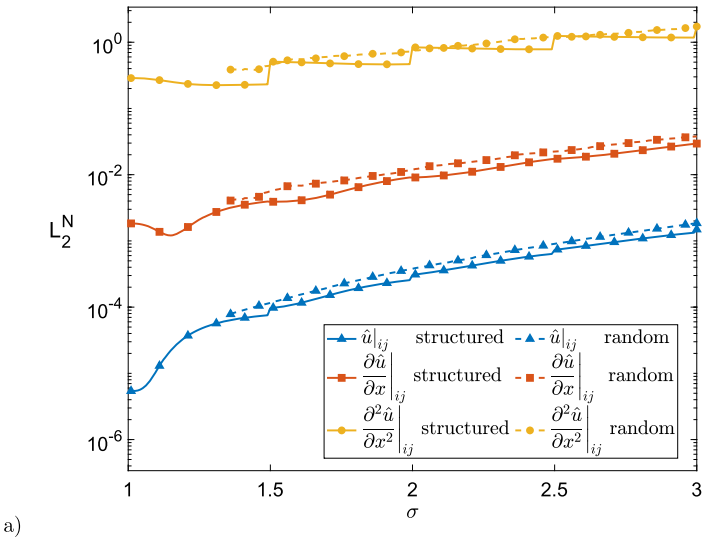

a)

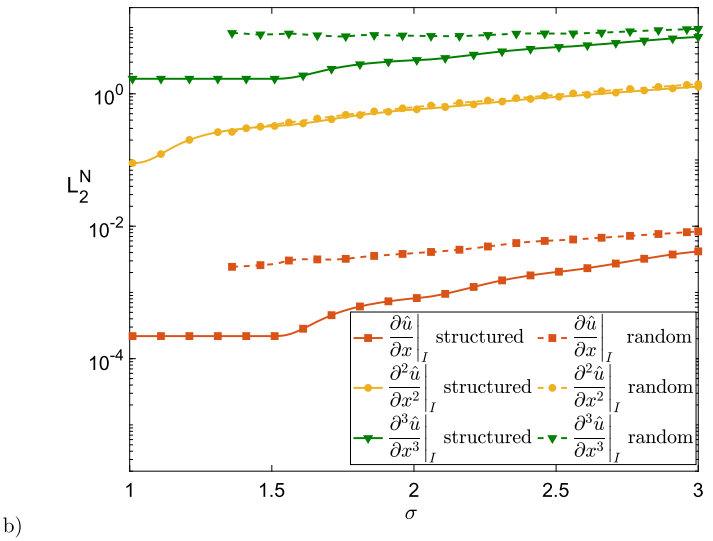

b)

Fig. 7. Accuracy and convergence 1D test: Parametric study of the smoothing length in terms of σ. Figure a) shows the obtained results at the integration point and in Figure b) the reconstruction is centered at the particle position.

For each particle distribution, denoted as N, we have computed the MLS reconstruction of the field function $u(x, y)$ at each integration point. Then the L_2^N norms of the errors of the reconstruction variable, the gradient modulus and the Laplacian of the variable at the integration point are computed and represented in Fig. 9 for $\sigma = 1.5$ and $\sigma = 2.0$.

Next, the derivatives of the field function are computed at each particle. The L_2^N norms of the errors of derivatives are computed and plotted in Fig. 10 for $\sigma = 1.5$ and $\sigma = 2.0$.

The expected order of accuracy is achieved in all cases.

4.2. Isentropic vortex convection

In the second test case, the numerical discretization of the Euler equations is tested. This test case corresponds to the convection of a vortex and it is widely used as benchmark case since it has analytical solution [32,40–42], that reads

$$\frac{u^x(x, y, t)}{a_\infty} = \frac{u^x_\infty}{a_\infty} - \frac{K}{2\pi a_\infty}\hat{y}e^{\alpha(1-r^2)/2}$$

$$\frac{u^y(x, y, t)}{a_\infty} = \frac{u^y_\infty}{a_\infty} + \frac{K}{2\pi a_\infty}\hat{x}e^{\alpha(1-r^2)/2}$$

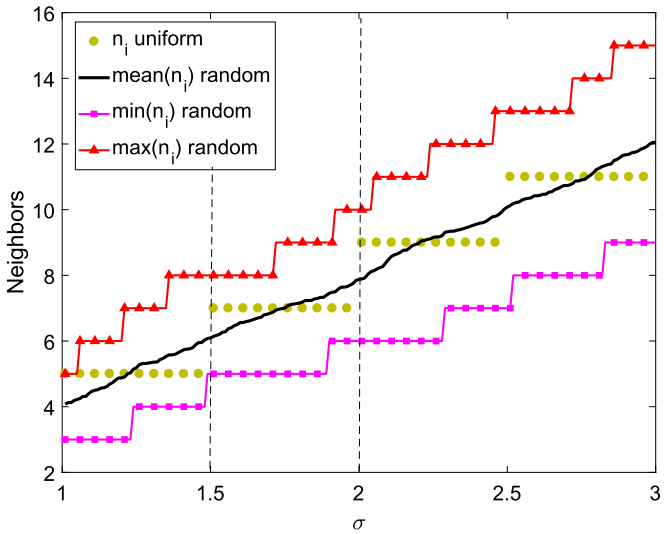

Fig. 8. Accuracy and convergence 1D test: Parametric study of the effect of the smoothing length parameter (σ) in the number of neighbors for uniform and random particles distributions.

$$\frac{T(x,y,t)}{T_\infty} = 1 - \frac{K^2(\gamma-1)}{8\alpha\pi^2 a_\infty^2} e^{\alpha(1-r^2)}$$
$$\frac{\rho(x,y,t)}{\rho_\infty} = \left(\frac{T(x,y,t)}{T_\infty}\right)^{\frac{1}{\gamma-1}}$$
$$\frac{p(x,y,t)}{p_\infty} = \left(\frac{T(x,y,t)}{T_\infty}\right)^{\frac{\gamma}{\gamma-1}}$$

where $\hat{x} = x - x_0 - u_\infty^x t$, $\hat{y} = y - y_0 - u_\infty^y t$ and $r = \sqrt{\hat{x}^2 + \hat{y}^2}$. The computational domain is a square $\Omega = [0, 10] \times [0, 10]$ with periodic boundary conditions. The chosen parameters are $\alpha = 1$, $\rho_\infty = 1$, $p_\infty = 1$, $(x_0, y_0) = (5, 5)$ and $K = 5$. For all the simulations the final time is $t = 5$.

Two configurations are analyzed in this test case: In the first configuration we set to null the convected velocity as $(u_\infty^x, u_\infty^y) = (0, 0)$, with this set of parameters the vortex rotates always around a fixed position $(x, y) = (5, 5)$. In the second configuration we set the convected velocity as $(u_\infty^x, u_\infty^y) = (2, 0)$, with this set of parameters the vortex starts at position $(x, y) = (5, 5)$ and at $t = 5$, due the periodic boundary conditions the vortex reaches again position $(x, y) = (5, 5)$.

For both configurations, we compute the test case with a set of uniform particles of 16^2, 32^2, 64^2 and 128^2 until the final time is achieved, where we compute the L_2^N norm of the error for the density field. The obtained results for the Eulerian and Lagrangian configurations are presented in Fig. 11.

The obtained results when an Eulerian configuration is chosen obtains orders of convergence higher than second. The theoretical formal order of the method is second at most [13]. This superconvergence is probably due to the high-order reconstruction of the variables, which guides the overall convergence of the scheme with these resolutions. Moreover, the formal order decreases in the last particle resolution in the convected vortex. On the other hand, when the Lagrangian configuration is used the formal order is drastically reduced to first order at most. Similar behaviors has been also observed in [43] for a different test case.

4.3. 2D viscous Taylor Green vortex

The next test case is the 2D Taylor Green Vortex. This test case is an exact time-dependent solution to the incompressible Navier-Stokes equations in 2D [44] and it is widely used to validate SPH methods [45,47]. The flow decays in time at a rate which is controlled by the viscosity. The analytical solution for the velocity and pressure fields corresponding to this flow in the domain $\Omega = [0, 2\pi] \times [0, 2\pi]$ is

$$u^x(x,y) = e^{\frac{-8\pi^2 t}{Re}} \cos(y) \sin(x) \tag{26}$$
$$u^y(x,y) = -e^{\frac{-8\pi^2 t}{Re}} \cos(x) \sin(y)$$
$$p(x,y) = \frac{e^{\frac{-16\pi^2 t}{Re}}}{4} (\cos(2x) + \cos(2y))$$

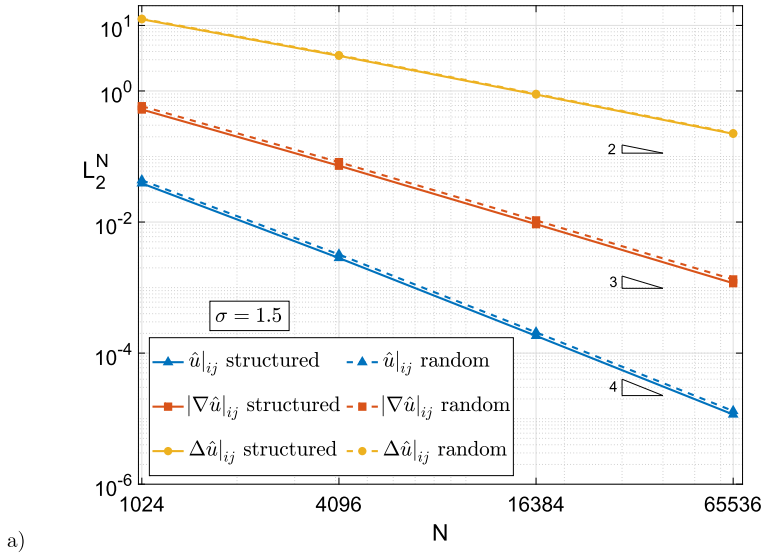

a)

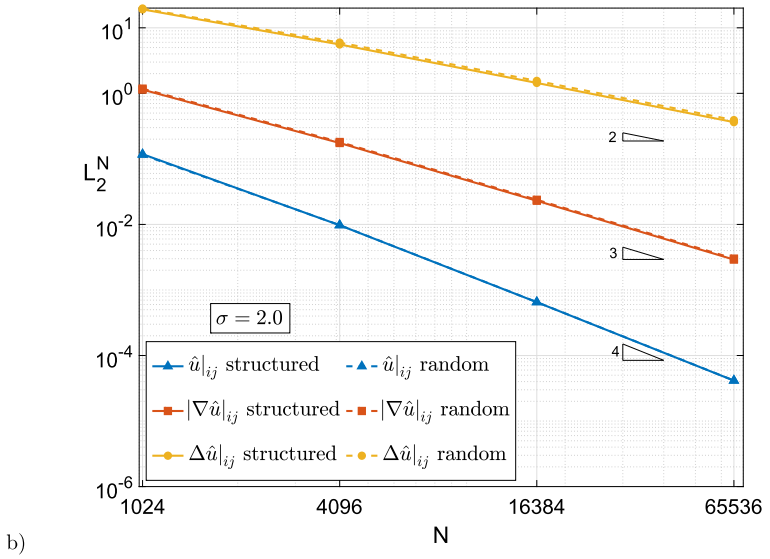

b)

Fig. 9. Accuracy and convergence 2D test: L_2^N norm of the committed error at the approximation of the variables and its derivatives at integrations points (midpoint between neighboring particles) for each discretization. N. Figure a) shows the obtained results with the parameter $\sigma = 1.5$ and Figure b) those obtained for $\sigma = 2.0$.

For Lagrangian particle methods this is a very challenging problem, since errors in the updating of the position of particles may lead the numerical scheme to reach a wrong solution. This fact will break the stationary closed trajectories which are obtained for the analytical solution. In this test case, the Reynolds number is set to 100. The computational domain Ω is discretized with 2500 particles disposed in a Cartesian distribution and periodic boundary conditions are imposed in all the boundaries. The initial configuration of particles and the initial velocity field are represented in Fig. 12 a). In this problem, a Lagrangian configuration is adopted and particle shifting is used as described in [23]. It is important to note that with the proposed methodology it is not required the use of procedures such as the particle packing method [22] to obtain a suitable initial distribution of the particles, which is required in SPH methods based on kernel approximations [22,29].

In Fig. 12, we plot the velocity magnitude at $t = 0$, $t = 1$ and $t = 2$. It is observed that the symmetry of the solution is kept, and the stationary closed trajectories are conserved.

In Fig. 13 the decay of the maximum velocity and the kinetic energy compared with the theoretical decay and with the results obtained with the δ^+-SPH method [46,47] are presented. The results obtained by the proposed method show a perfect match with the theoretical curve. Note also that both, the Eulerian and the Lagrangian configurations, obtains similar results.

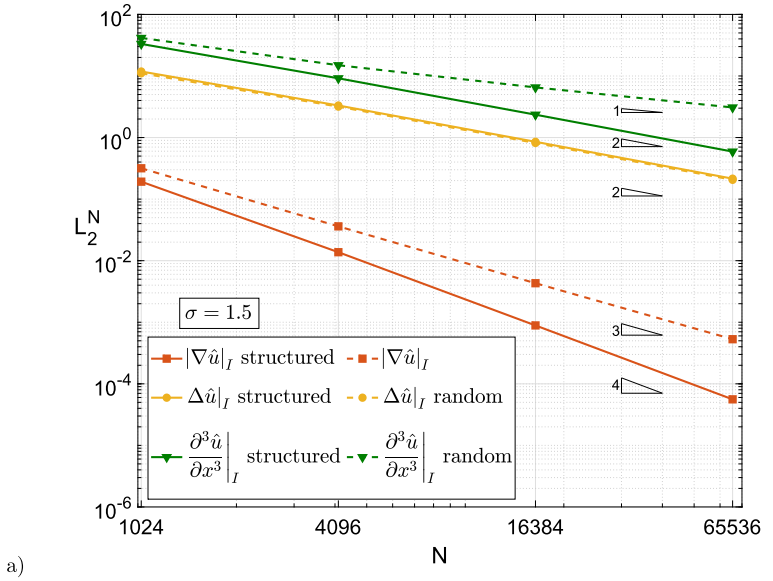

a)

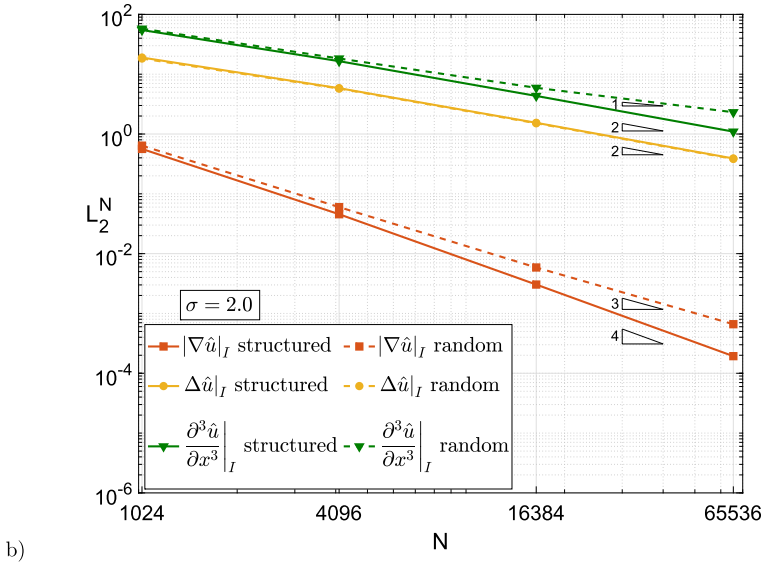

b)

Fig. 10. Accuracy and convergence 2D test: L_2^N norm of the committed error of the derivatives at the particles position for each particle discretization N. Figure a) shows the obtained results with the parameter $\sigma = 1.5$ and Figure b) those obtained for $\sigma = 2.0$.

4.4. Steady $Re = 40$ flow around a 2D cylinder

In this test case, we consider the flow around a circular cylinder as a validation case of the proposed method for viscous flows with curved walls. The setup of this test case is as follows: The radius of the cylinder is $R = 0.5$, the Reynolds number is $Re = 40$ and the free-stream Mach number is $M_\infty = 0.1$.

The computational domain is discretized with a total number of 10800 particles and 120 particles around the cylinder. Fig. 14 shows a close view of the particle distribution around the cylinder. Free-stream variables are fixed at the outer boundary and we impose the no-slip and adiabatic boundary conditions at the cylinder solid wall. We solve the problem in an Eulerian configuration until the steady state is obtained. In Fig. 15 the velocity field and the streamlines are plotted near the cylinder. It is observed that the solution obtained using the proposed numerical method is able to obtain good symmetry of the vortices created downstream the cylinder.

In Fig. 16 the pressure coefficient distribution C_p around the cylinder is plotted at the steady state. The solution is compared with a reference solution obtained on a 3^{rd}-order finite volume scheme using a grid with the same spatial resolution than the present particle discretization [32]. It is observed that the proposed approach results are in excellent agreement with the reference solution.

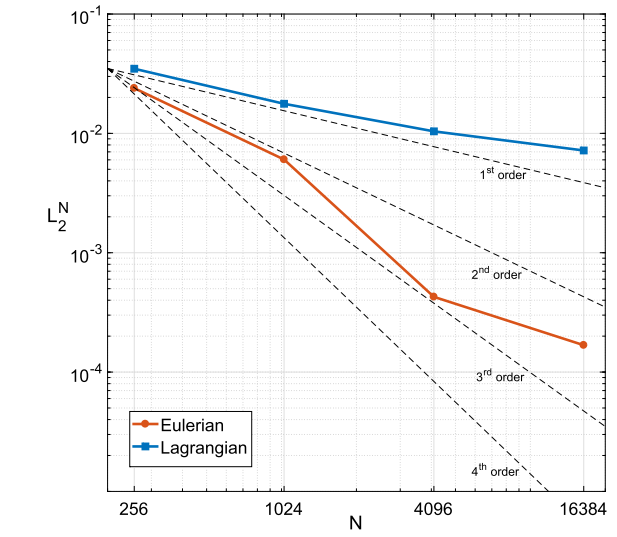

a)

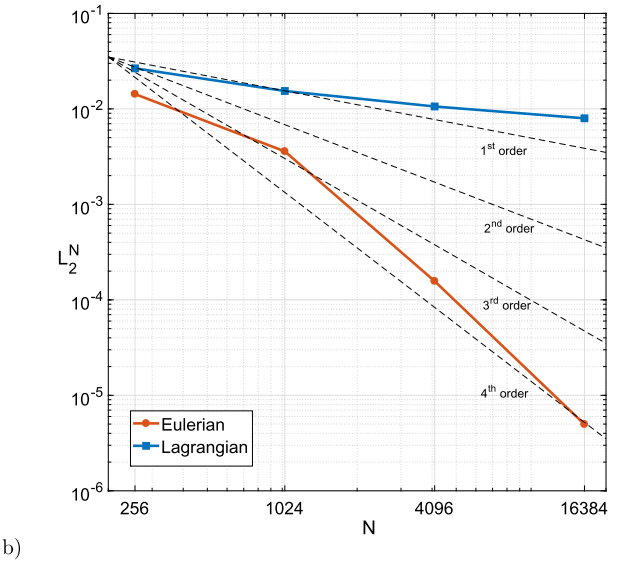

b)

Fig. 11. Isentropic vortex convection: L_2^N norm of the committed error in the density field for both Lagrangian and Eulerian configurations for different particle resolutions, N. Figure a) shows the obtained results for the convected vortex and Figure b) shows the results for the stationary vortex.

The drag coefficient C_D and the front and back pressure coefficients ($C_p(0)$ and $C_p(\pi)$) are compared in Table 1 with reference values from the literature. It is observed that the proposed approach obtains results comparable to those obtained in the literature. In particular, they are in excellent agreement with the ones obtained with a 3rd-order finite volume scheme using a grid with the same spatial resolution [32].

4.5. Unsteady flow around a 2D cylinder $Re = 100$ and $Re = 185$

In this test case, we address the simulation of a non-steady viscous flow past a two-dimensional cylinder. The domain and the particle distribution is the same than the used in the previous case. An Eulerian configuration is chosen. Now, two different Reynolds number are addressed, namely $Re = 100$ and $Re = 185$. This configuration leads to a flow with a periodic pattern of swirling vortices originated at cylinder wall.

Figs. 17 and 18 show the temporal evolution of the drag and lift coefficients and the vorticity field respectively for the two different Reynolds numbers addressed. It is clearly observed the periodic pattern of vortices appearing downstream the cylinder.

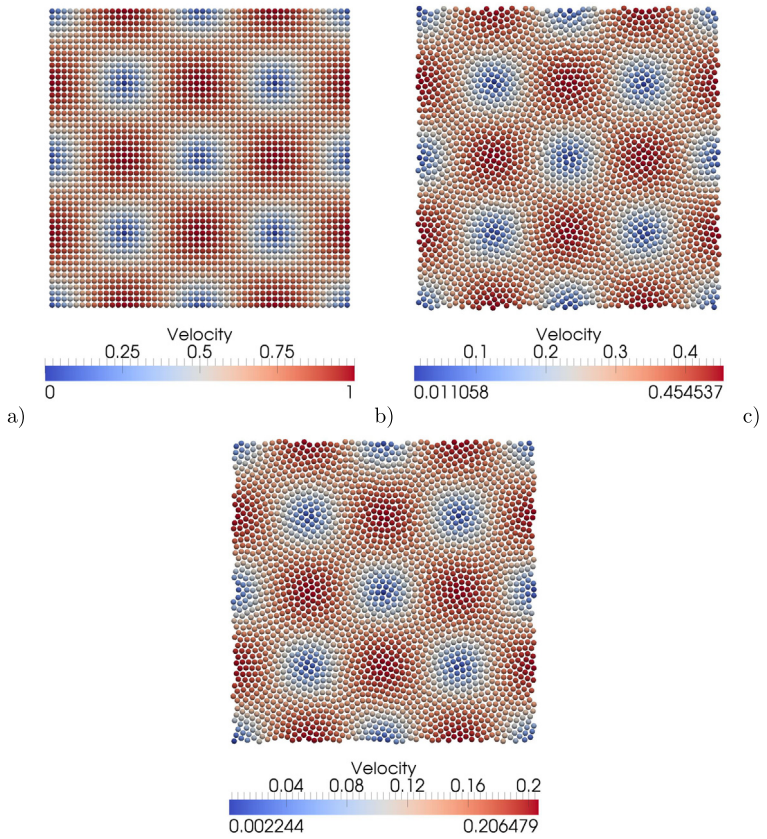

Fig. 12. 2D Taylor Green flow for $Re = 100$. Figures a), b) and c) represent velocity magnitude at $t = 0$, $t = 1$ and $t = 2$.

Table 2 compares the drag and lift coefficients and the Strouhal number obtained using the proposed method with the results obtained by several authors. It is observed that the results obtained are comparable to those obtained using other methods.

4.6. Decay of compressible isotropic turbulence

In this numerical example, we extend the proposed formulation to 3D to analyze the decay of compressible isotropic turbulence. This test case is commonly used to verify the ability of the numerical method to simulate turbulent flow. Many authors have used this numerical test to develop new subgrid scale models and to analyze numerical methods [62–66].

4.6.1. Setup of the problem

A periodic $2\pi \times 2\pi \times 2\pi$ cube is considered for the computational domain and it is discretized using an homogeneous distribution of particles. Periodic boundary conditions are considered for all the boundaries and an Eulerian configuration is chosen. As it is usual in this problem, the flow is defined by the turbulent Mach number (M_t) and Taylor's micro-scale Reynolds number (Re_λ)

$$M_t = \frac{\sqrt{\langle u_i' u_i' \rangle}}{\langle c \rangle} \tag{27}$$

$$Re_\lambda = \frac{\langle \rho \rangle \, u'_{\text{rms}} \lambda}{\mu} \tag{28}$$

where the notation $\langle\rangle$ refers to mean value and primes denote fluctuating variables. The root mean square of the velocity (u_{rms}) is defined as

$$u_{\text{rms}} = \sqrt{\frac{\langle u_i' u_i' \rangle}{3}} \tag{29}$$

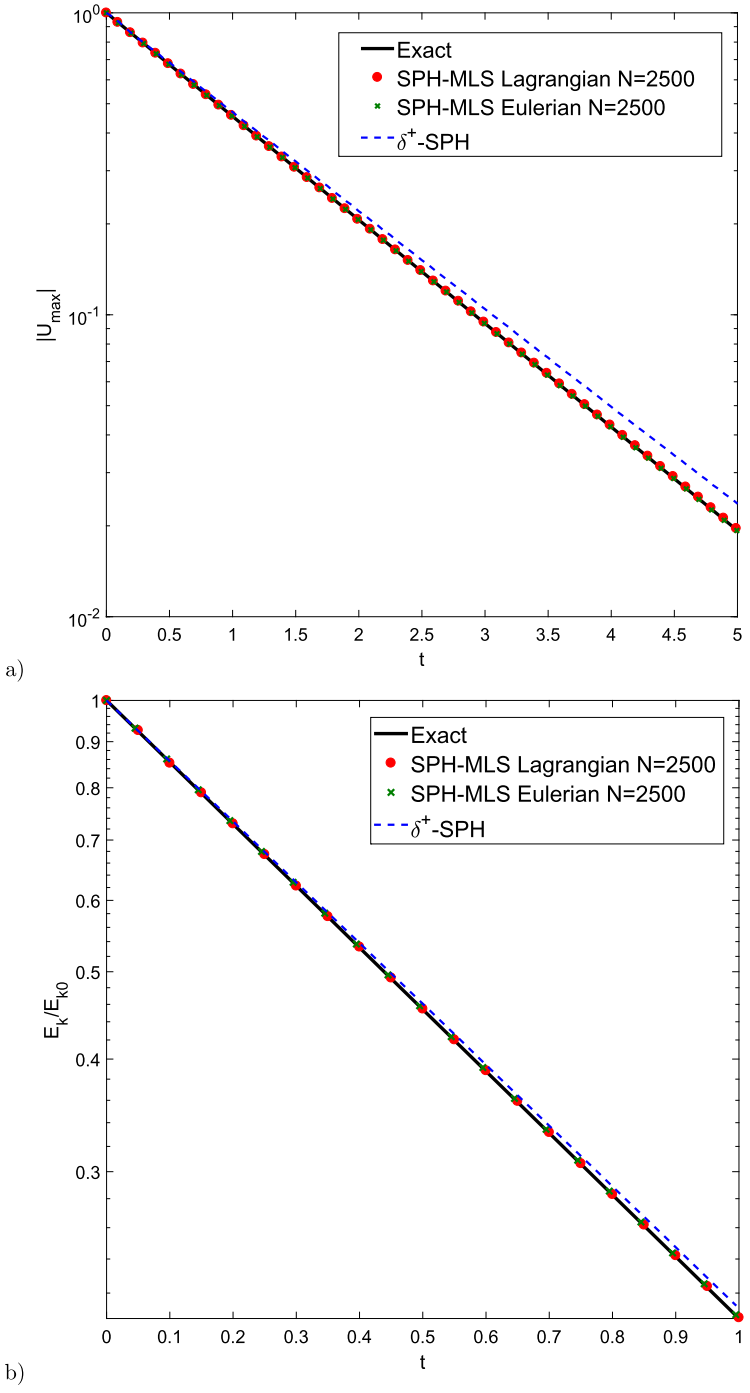

Fig. 13. 2D Taylor Green flow for $Re = 100$. a) Time evolution of the maximum velocity magnitude over time compared with the exact solution and the δ^+-SPH results from [46] and b) time evolution of the kinetic energy compared with the analytical solution and the δ^+-SPH results from [47].

The initial conditions are defined following a given initial three-dimensional kinetic energy spectrum as

$$E_{3D} \sim k^4 \exp\left[-2\left(\frac{k}{k_0}\right)^2\right] \tag{30}$$

where k is the magnitude of the wave number vector, and $k_0 = 4$ is the wavenumber at the peak of the spectrum.

In this case, the initial velocity fluctuations are parametrized by the turbulent Mach number and also by the fraction of energy in the dilatational part of the velocity, $\chi = 0.2$ [67]. The initial turbulent Mach number is taken as $M_{t,0} = 0.4$

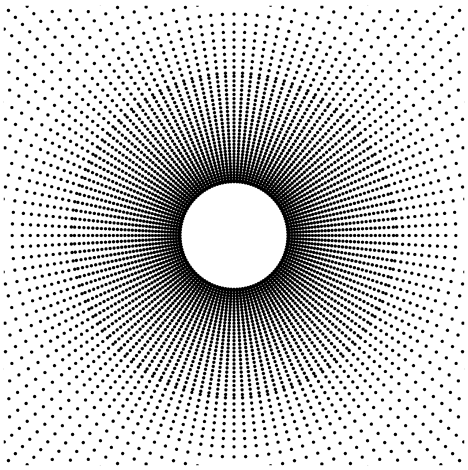

Fig. 14. Steady $Re = 40$ flow around a 2D cylinder. Particle distribution around the cylinder.

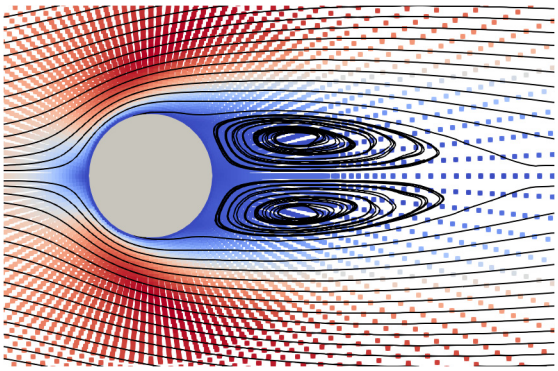

Fig. 15. Steady $Re = 40$ flow around a 2D cylinder. Velocity field and streamlines around the cylinder.

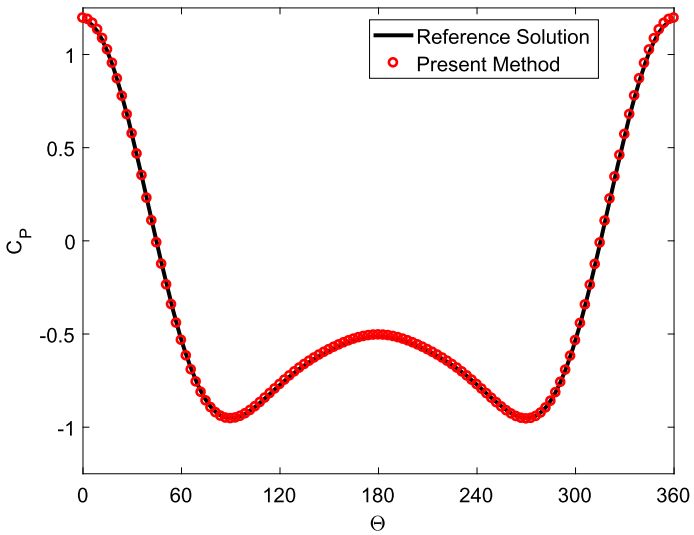

Fig. 16. Steady $Re = 40$ flow around a 2D cylinder. Comparison of the pressure coefficient (C_p) distribution around the cylinder obtained using the proposed method and a 3rd-order finite volume with the same spatial resolution [32].

Table 1
Steady $Re = 40$ flow around a 2D cylinder. Comparison of the drag coefficient C_D, front and back pressure coefficients ($C_p(0)$ and $C_p(\pi)$) obtained using the SPH-MLS scheme and other computations using grid methods [32,48], lattice Boltzmann methods [49,50] and SPH methods [51].

Method	C_D	$C_p(0)$	$C_p(\pi)$
Present Method	1.570	−0.505	1.195
Ramirez et al. [32]	1.568	−0.512	1.180
Chassaing et al. [48]	1.565	−0.516	1.205
Niu et al. [49]	1.574	−0.555	1.147
He and Doolen [50]	1.499	−0.487	1.133
Marrone et al. [51]	1.6	–	–

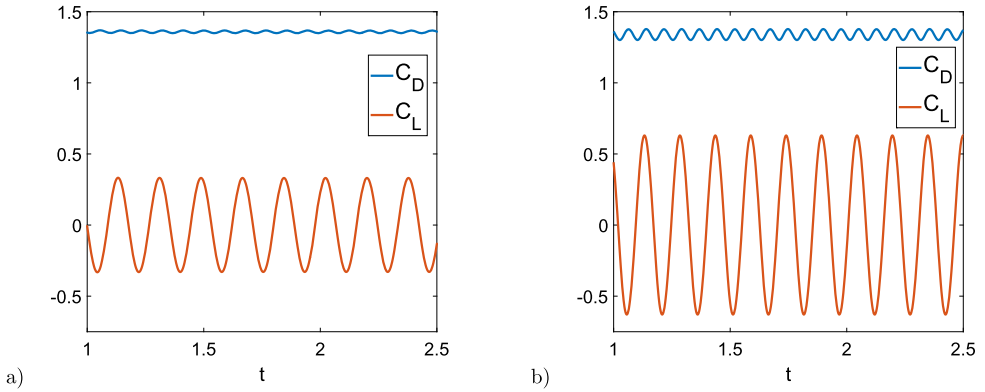

Fig. 17. Unsteady flow around a 2D cylinder $Re = 100$ and $Re = 185$. Temporal evolution of the drag and lift coefficients, a) $Re = 100$ and b) $Re = 185$.

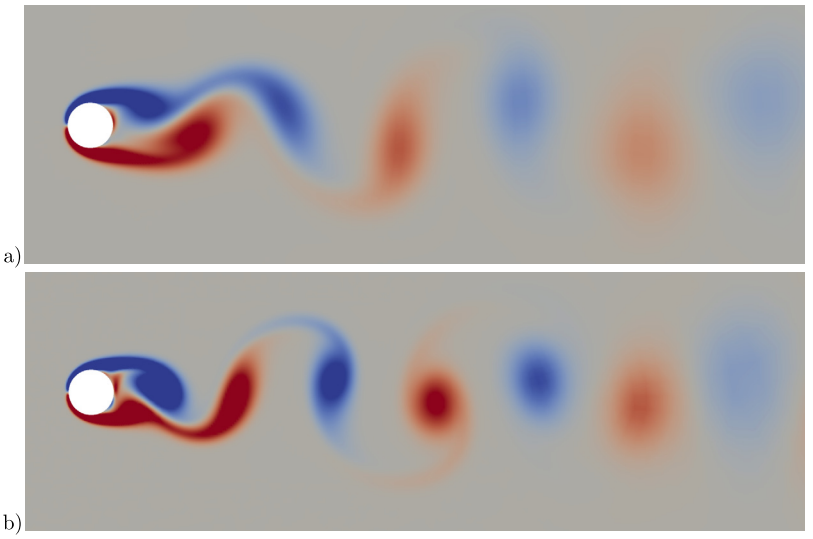

Fig. 18. Unsteady flow around a 2D cylinder $Re = 100$ and $Re = 185$. Vorticity field, a) $Re = 100$ and b) $Re = 185$.

and the initial Taylor's microscale Reynolds number is chosen as $Re_{\lambda,0} = 2157$, which corresponds with a Reynolds number $Re = 536.9$. The setup presented here corresponds to the case 6 of [64].

With this configuration, the initial density and temperature fields are given by

$$\begin{aligned} \left(\rho'_{rms}\right)^2 / \langle\rho\rangle^2 &= 0.032 \\ \left(T'_{rms}\right)^2 / \langle T\rangle^2 &= 0.005 \end{aligned} \tag{31}$$

The evolution of the flow with this initial conditions leads to a nonlinear subsonic regime [68] and weak shocklets develop spontaneously from the turbulent motion. Three different particle discretizations are used in this test case: 32^3, 64^3 and 128^3 particles.

Table 2
Unsteady flow around a 2D cylinder $Re = 100$ and $Re = 185$. Comparison of mean drag coefficient $\bar{C_D}$, mean and rms lift coefficients (C_L and $C_{L,rms}$) obtained using the SPH-MLS scheme and other computations using grid-based [52,53,57,58], immersed boundary [54–56,60], ALE [61] and SPH methods [51,59].

Method	$Re = 100$			$Re = 185$		
	$\overline{C}_D$	C_L	S_t	$\overline{C}_D$	$C_{L,rms}$	S_t
Present Method	1.3587	±0.3325	0.1653	1.3398	0.4447	0.1937
Liu et al. [52]	1.350	±0.339	0.165	–	–	–
Rajani et al. [53]	1.3353	–	0.1569	–	–	–
Marrone et al. [51]	1.36	±0.24	0.168	–	–	–
Ng et al. [54]	1.368	±0.360	–	–	–	–
Constant et al. [55]	1.37	–	0.165	1.379	0.427	0.198
Vanella and Balaras [56]	–	–	–	1.377	0.461	–
Guilmineau and Queutey [57]	–	–	–	1.287	0.443	0.195
Lu and Dalton [58]	–	–	–	1.31	0.422	0.195
Liu et al. [59]	–	–	–	1.372	0.427	–
Sun et al. [47]	–	–	–	1.363	–	0.196
Liu et al. [60]	–	–	–	1.289	0.451	0.197

We run this test case using a time step of $\Delta t = 0.05$ with the 32^3 particle distribution. This corresponds to 250 time-steps per eddy turnover time τ, that is $\tau = 12.5$ for this configuration. For the 64^3 and 128^3 particle distributions we keep the CFL constant. In Fig. 19 we show the results obtained with the present approach in terms of the time evolution of the kinetic energy and the mean square density fluctuations. The results are compared with a reference solution computed with a sixth-order compact finite difference scheme, with explicit filtering using a tenth-order Padé filter [69]. This solution follows closely the results of a DNS.

The decay of kinetic energy is plotted in Fig. 19 a). The coarser discretization shows excessive dissipation. However, it can be seen that as the number of particles is increased, the results converge to the reference solution, and the results obtained for 128^3 particles are in excellent agreement with those of the reference solution. The results obtained for the density fluctuations follow the same trend, as shown in Fig. 19 b). Fig. 20 a) shows that the proposed scheme is able to reproduce the thermodynamic variables of the flow. This is a remarkable result, since some methods are not able to simultaneously predict the correct scaling and decay rates of thermodynamic variables [70].

The instantaneous three-dimensional energy spectra ($E(k) = \rho((u^x)^2 + (u^y)^2 + (u^z)^2)$) at $t/\tau = 0.3$ is plotted in Fig. 20 b). The results reproduce correctly the reference spectrum, although some overdissipation is found in the highest scales for the coarser grid. It is also observed that the proposed scheme is able to reproduce the two different slopes appearing in the energy spectrum, which agrees with the Eddy-Damped Quasi-Normal Markovian Theory (EDQNM) [71]. As the number of particles is increased, the spectrum converges to the reference. It is important to note that no piling-up of energy is detected.

In Fig. 21 the Q-criterion iso-surface with a value of 0.25 is compared at $t = 10$ for the different particle resolutions. It can be noted the effect of the particle resolution.

4.7. 3D Taylor Green vortex

The 3D Taylor-Green vortex (TGV) test case is commonly used to test the accuracy and performance of numerical methods on the direct numerical simulation of a three-dimensional periodic and transitional flow. The computational domain is the cube defined as $[0, 2\pi] \times [0, 2\pi] \times [0, 2\pi]$ with periodic boundary conditions.

Two different test cases are analyzed here. The inviscid TGV and a viscous TGV with a Reynolds number $Re = 1600$. These test cases are solved using three different particle distributions with 32^3, 64^3, and 128^3 particles, until a final time of $t = 10$ under an Eulerian configuration.

4.7.1. TGV: inviscid test case

The initial condition of the inviscid TGV is defined as

$$
\begin{aligned}
u^x(x, y, z, 0) &= \sin(x)\cos(y)\cos(z) \\
u^y(x, y, z, 0) &= -\cos(x)\sin(y)\cos(z) \\
u^z(x, y, z, 0) &= 0 \\
\rho(x, y, z, 0) &= 1 \\
p(x, y, z, 0) &= 100 + \frac{1}{16}[(\cos(2x) + \cos(2y))(2 + \cos(2z)) - 2]
\end{aligned}
\tag{32}
$$

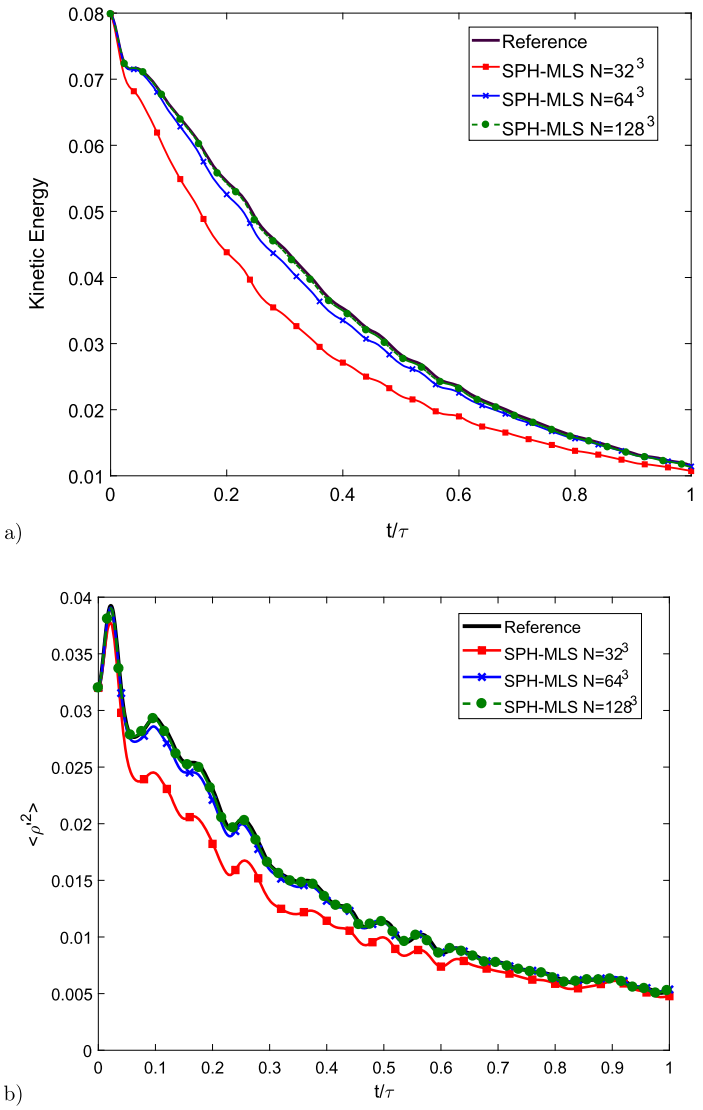

Fig. 19. Decay of homogeneous isotropic turbulence. Time evolution of kinetic energy (top) and mean square density fluctuations (bottom). The reference solution was computed following [69].

In this test case, the ratio of specific heat is $\gamma = 5/3$. The inviscid case is equivalent to an infinite Reynolds number. Ideally, in this test case, there is no decay of the kinetic energy. However, since the numerical method introduces some dissipation, all the dissipation comes from the numerical scheme. When the flow scales are smaller enough, the solution becomes under resolved, and dissipation (and also dispersion) errors are introduced by the numerical scheme. The numerical dissipation introduced by the numerical scheme starts a decay process which ideally should follow the (-5/3) decay Kolmogorov's law. The evolution of the kinetic energy and enstrophy obtained by the proposed scheme are plotted in Fig. 22 a), and compared with the results obtained by the classical finite difference WENO5 scheme [72,73], with a reference solution obtained by [74] with a very fine grid (8192^3) and the semi-analytic results of [75].

It can be seen that the proposed meshless method converges to the Reference solution as the number of particles is increased. Moreover, it obtains more accurate results than the WENO5 scheme. An important result is that the slope of the kinetic energy decay is similar to that of the reference solution. The enstrophy levels are also larger than those obtained by the WENO5 scheme, indicating the presence of more energetic vortices in the solution obtained by the SPH-MLS scheme.

4.7.2. TGV: viscous case with $Re = 1600$

Finally, we present the results for the viscous TGV. The initial condition for this test case is a slight variation of that of the inviscid case to match the case description provided in [76].

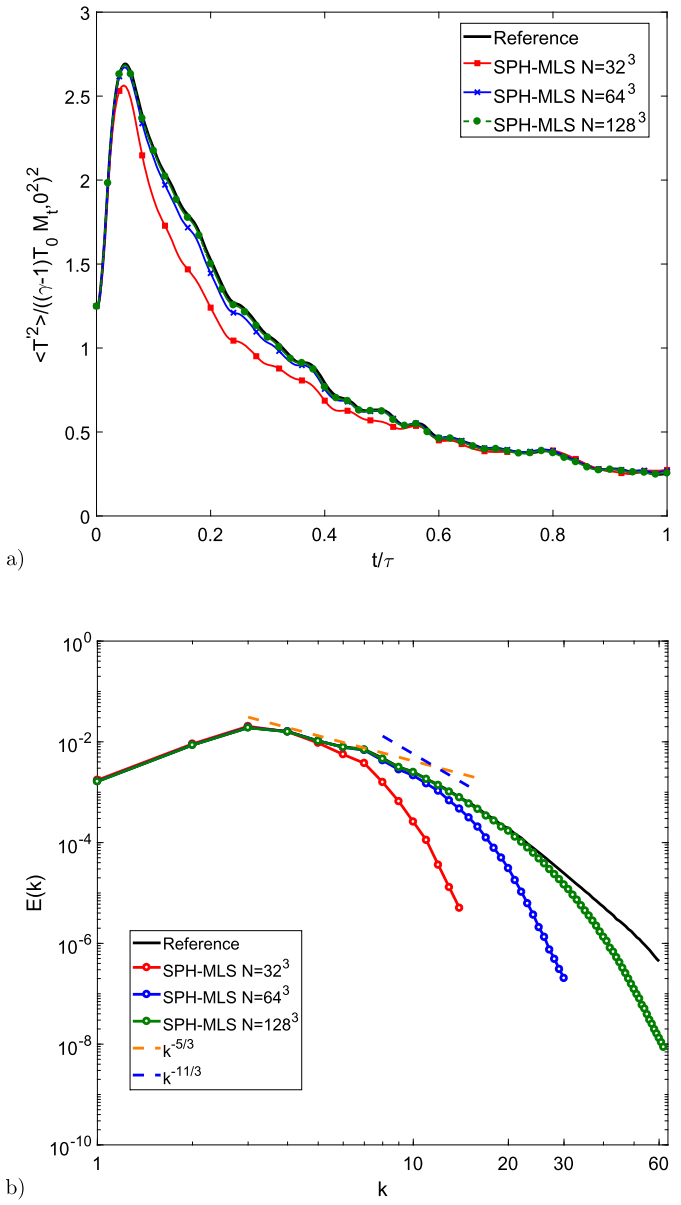

Fig. 20. Decay of homogeneous isotropic turbulence. Time evolution of normalized temperature fluctuations (top) and instantaneous three-dimensional energy spectra at $t/\tau = 0.3$ (bottom). The reference solution was computed following [69].

$$
\begin{aligned}
u^x(x, y, z, 0) &= \sin(x)\cos(y)\cos(z) \\
u^y(x, y, z, 0) &= -\cos(x)\sin(y)\cos(z) \\
u^z(x, y, z, 0) &= 0 \\
p(x, y, z, 0) &= \frac{1}{\gamma M_0^2} + \frac{1}{16}\left[(\cos(2x) + \cos(2y))(2 + \cos(2z)) - 2\right] \\
\rho(x, y, z, 0) &= \gamma M_0^2 p(x, y, z, 0)
\end{aligned}
\tag{33}
$$

A uniform dimensionless temperature field of unity has been assumed along with the perfect gas relation. The reference Mach number is chosen as $M_0 = 0.1$ to minimize compressibility effects. A constant Prandtl number of $Pr = 0.71$, $\gamma = 1.4$ and a Reynolds number of $Re = 1600$ are used. With this setup, the flow evolves and smaller scales progressively appear, until the flow transitions to turbulence and decays in a similar way to decaying homogeneous turbulence.

The evolution of the kinetic energy and enstrophy obtained by the proposed scheme are plotted in Fig. 23, and compared with the results obtained by the WENO5 scheme [72] and the DNS solution presented in [76].

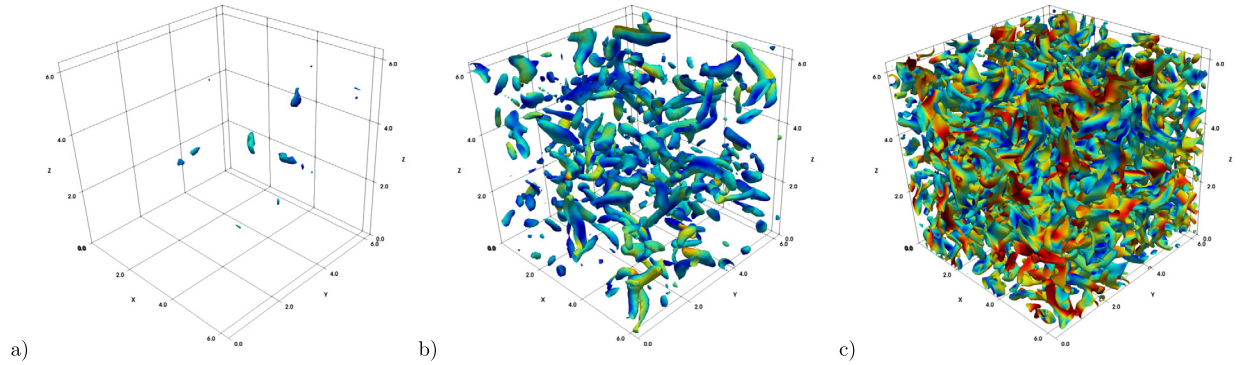

Fig. 21. Decay of homogeneous isotropic turbulence. Iso-surfaces of Q-Criterion $= 0.25$ at $t = 10$, where a) is obtained with 32^3 particles, b) with 64^3 particles and c) with 128^3 particles.

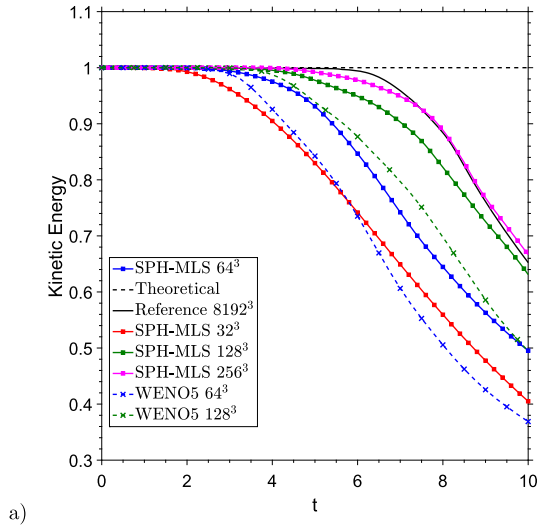

a)

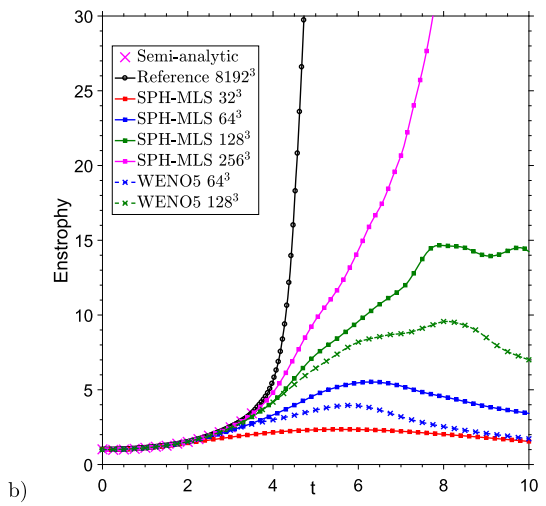

b)

Fig. 22. 3D inviscid Taylor Green: Time evolution of the kinetic energy a) and the enstrophy b).

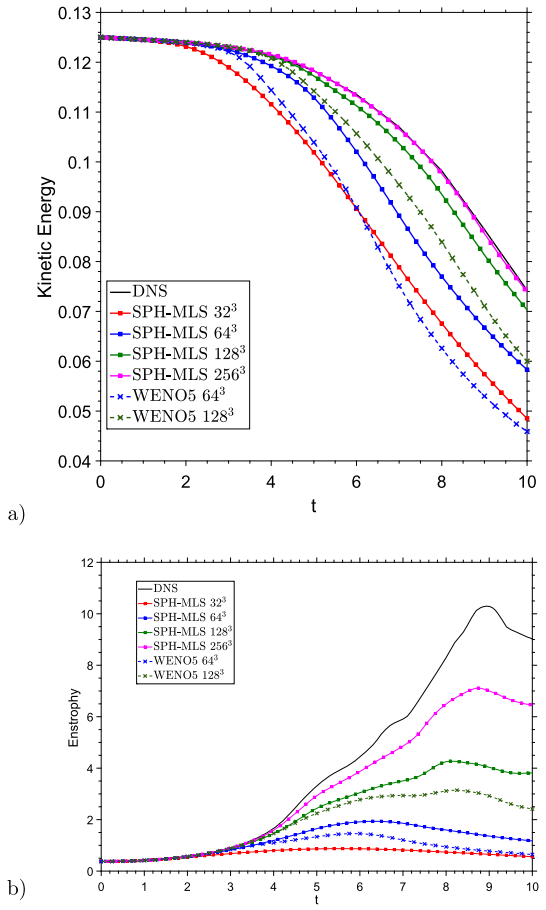

Fig. 23. 3D viscous Taylor Green: Time evolution of the kinetic energy a) and the enstrophy b).

As in the previous case, the solution converges to the DNS solution as the particle distribution is increased, and it obtains consistently more accurate results than the WENO5 scheme for both, the decay of kinetic energy and the enstrophy evolution. In Fig. 24 shows the time evolution of the Q-Criterion from $t = 0$ to $t = 10$ with the finer particle resolution. It can be noted the flow transition from laminar with vortex-tubes into small-scale turbulence.

5. Conclusions

In this work we have proposed a high-accurate meshless discretization to solve the compressible Navier-Stokes equations. The standard kernel approximation is completely substituted by MLS approximations. In addition, the MLS approximations are also used to obtain a high-order reconstruction of the Riemann states instead of Taylor polynomials. The proposed method presents several advantages compared with standard kernel approximations. It ensures the verification of the partition of unity even in regions close to the boundaries. Moreover, shape function derivatives form a partition of nullity, which avoids problems related with the initial configuration of particles. The use of MLS functions in the reconstruction as well the integration weights leads to meshless schemes with greater accuracy and smaller stencils than traditional SPH discretization with kernel approximations. We have shown that the proposed method is able to obtain comparable results to those obtained with grid-based methods in different regimes of viscous flow problems.

CRediT authorship contribution statement

Luis Ramírez: Conceptualization, Formal analysis, Funding acquisition, Methodology, Project administration, Resources, Supervision, Validation, Writing – original draft, Writing – review & editing. **Antonio Eirís:** Investigation, Methodology, Software, Validation, Writing – original draft. **Iván Couceiro:** Investigation, Software, Validation, Visualization. **José París:** Data curation, Formal analysis, Investigation, Software. **Xesús Nogueira:** Conceptualization, Formal analysis, Funding acquisition, Methodology, Project administration, Resources, Supervision, Writing – review & editing.

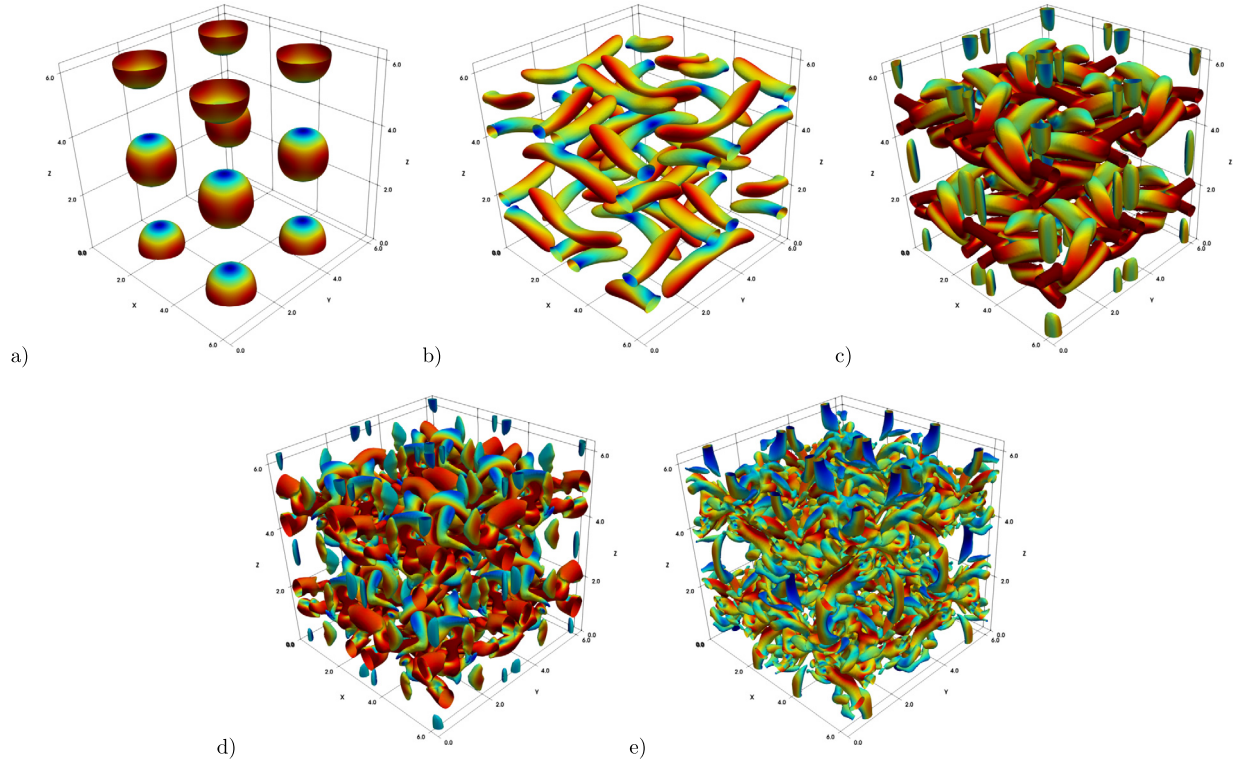

Fig. 24. 3D viscous Taylor Green: Iso-surfaces of Q-Criterion with a value of 0.5: a) at $t = 0$, b) at $t = 2.5$, c) at $t = 5$, d) at $t = 7.5$ and e) at $t = 10$ with 128^3 particles.

Declaration of competing interest

The authors declare that they have no known competing financial interests or personal relationships that could have appeared to influence the work reported in this paper.

Acknowledgements

This work has been partially supported by *Ministerio de Ciencia, Innovación y Universidades* of the Spanish Government (grant #RTI2018-093366-B-I00) and by the *Consellería de Educación e Ordenación Universitaria* of the *Xunta de Galicia* (grant# ED431C 2018/41), cofinanced with FEDER funds of the European Union. Luis Ramírez also acknowledges the funding provided by the *Xunta de Galicia* through the program *Axudas para a mellora, creación, recoñecemento e estruturación de agrupacións estratéxicas do Sistema universitario de Galicia* (reference # ED431E 2018/11).

References

[1] R. Vacondio, C. Altomare, M.D. Leffe, X. Hu, D.L. Touzé, S. Lind, J.C. Marongiu, S. Marrone, B. Rogers, A. Souto-Iglesias, Grand challenges for smoothed particle hydrodynamics numerical schemes, Comput. Part. Mech. 8 (2020) 575–588.
[2] J.P. Vila, On particle weighted methods and smooth particle hydrodynamics, Math. Models Methods Appl. Sci. 09 (02) (1999) 161–209.
[3] B. Ben Moussa, On the convergence of SPH method for scalar conservation laws with boundary conditions, Methods Appl. Anal. 13 (2006) 29–62.
[4] M. Junk, Do finite volume methods need a mesh?, in: Meshfree Methods for Partial Differential Equations, Springer, 2003, pp. 223–238.
[5] M. Schaller, R.G. Bower, T. Theuns, On the use of particle based methods for cosmological hydrodynamical simulations, in: 8th International SPHERIC Workshop, Trondheim, Norway, 2013.
[6] D. Hietel, K. Steiner, J. Struckmeier, A finite-volume particle method for compressible flows, Math. Models Methods Appl. Sci. 10 (09) (2000) 1363–1382.
[7] N. Ivanova, S. Justham, X. Chen, O.D. Marco, C.L. Fryer, E. Gaburov, H. Ge, E. Glebbeek, Z. Han, X.D. Li, G. Lu, T. Marsh, Ph. Podsiadlowski, A. Potter, N. Soker, R. Taam, T.M. Tauris, E.P.J. van den Heuvel, R.F. Webbink, Common envelope evolution: where we stand and how we can move forward, Astron. Astrophys. Rev. 21 (1) (2013).
[8] J.J. Monaghan, SPH compressible turbulence, Mon. Not. R. Astron. Soc. 335 (3) (2002) 843–852.
[9] J.J. Monaghan, A turbulence model for smoothed particle hydrodynamics, Eur. J. Mech. B, Fluids 30 (4) (2011) 360–370.
[10] A. Mayrhofer, D. Laurence, B. Rogers, D. Violeau, DNS and LES of 3-D wall-bounded turbulence using smoothed particle hydrodynamics, Comput. Fluids 115 (2015) 86–97.
[11] X. Hu, N. Adams, A SPH model for incompressible turbulence, Proc. IUTAM 18 (2015) 66–75.
[12] A. Di Mascio, M. Antuono, A. Colagrossi, S. Marrone, Smoothed particle hydrodynamics method from a large eddy simulation perspective, Phys. Fluids 29 (2017) 035102.

[13] L. Ramírez, X. Nogueira, S. Khelladi, A. Krimi, I. Colominas, A very accurate arbitrary Lagrangian-Eulerian meshless method for computational aeroacoustics, Comput. Methods Appl. Mech. Eng. 342 (2018) 116–141.
[14] P. Lancaster, K. Salkauskas, Surfaces generated by moving least squares methods, Math. Comput. 37 (155) (1981) 141.
[15] W.K. Liu, W. Hao, Y. Chen, S. Jun, J. Gosz, Multiresolution reproducing kernel particle methods, Comput. Mech. 20 (4) (1997) 295–309.
[16] D. Avesani, M. Dumbser, A. Bellin, A new class of Moving-Least-Squares WENO-SPH schemes, J. Comput. Phys. 270 (2014) 278–299.
[17] X. Nogueira, L. Ramírez, S. Clain, R. Loubère, L. Cueto-Felgueroso, I. Colominas, High-accurate SPH method with Multidimensional Optimal Order Detection limiting, Comput. Methods Appl. Mech. Eng. 310 (2016) 134–155.
[18] D. Avesani, M. Dumbser, R. Vacondio, M. Righetti, An alternative SPH formulation: ADER-WENO-SPH, Comput. Methods Appl. Mech. Eng. 382 (2021) 113871.
[19] E. Oñate, S. Idelshon, O.C. Zienkiewicz, R.L. Taylor, A finite point method in computational mechanics. Applications to convective transport and fluid flow, Int. J. Numer. Methods Eng. 39 (22) (1996) 3839–3866.
[20] E. Oñate, Derivation of stabilized equations for numerical solution of advective-diffusive transport and fluid flow problems, Comput. Methods Appl. Mech. Eng. 151 (1998) 233–265.
[21] E. Ortega, E. Oñate, S. Idelsohn, A finite point method for adaptive three-dimensional compressible flow calculations, Int. J. Numer. Methods Fluids 60 (2009) 937–971.
[22] A. Colagrossi, B. Bouscasse, M. Antuono, S. Marrone, Particle packing algorithm for SPH schemes, Comput. Phys. Commun. 183 (8) (2012) 1641–1653.
[23] R.M. Nestor, M. Basa, M. Lastiwka, N.J. Quinlan, Extension of the finite volume particle method to viscous flow, J. Comput. Phys. 228 (2009) 1733–1749.
[24] B. Nayroles, G. Touzot, P. Villon, Generalizing the finite element method diffuse approximation and diffuse elements, Comput. Mech. 10 (1992) 307–318.
[25] T. Belystschko, Y.Y. Lu, L. Gu, Element-free Galerkin methods, Int. J. Numer. Methods Eng. 37 (1994) 229–256.
[26] G. Dilts, Moving-least-squares-particle hydrodynamics. Consistency and stability, Int. J. Numer. Methods Eng. 44 (8) (1999) 1115–1155.
[27] G. Dilts, Moving-least-squares-particle hydrodynamics. Conservation and boundaries, Int. J. Numer. Methods Eng. 48 (10) (2000) 1503–1524.
[28] J.P. Morris, A study of the stability properties of smooth particle hydrodynamics, Publ. Astron. Soc. Aust. 13 (1) (1996) 97–105.
[29] A. Eirís, L. Ramírez, J. Fernandez-Fidalgo, I. Couceiro, X. Nogueira, SPH-ALE scheme for weakly compressible viscous flow with a posteriori stabilization, Water 13 (3) (2021) 245.
[30] D. Avesani, M. Dumbser, G. Chiogna, A. Bellin, An alternative smooth particle hydrodynamics formulation to simulate chemotaxis in porous media, J. Math. Biol. 74 (2017) 1037–1058.
[31] X. Zheng, Q. Ma, S. Shao, Study on SPH viscosity term formulations, Appl. Sci. 8 (2018) 249.
[32] L. Ramírez, X. Nogueira, P. Ouro, F. Navarrina, S. Khelladi, I. Colominas, A higher-order chimera method for finite volume schemes, Arch. Comput. Methods Eng. 25 (3) (2017) 691–706.
[33] S. Marrone, M. Antuono, A. Colagrossi, G. Colicchio, D.L. Touzé, G. Graziani, δ-SPH model for simulating violent impact flows, Comput. Methods Appl. Mech. Eng. 200 (2011) 1526–1542.
[34] Z. Chen, Z. Zong, H.T. Li, J. Li, An investigation into the pressure on solid walls in 2D sloshing using SPH method, Ocean Eng. 59 (2013) 129–141.
[35] J.S. Chen, M. Hillman, S.W. Chi, Meshfree methods: progress made after 20 years, J. Eng. Mech. 143 (4) (2017) 04017001.
[36] L. Cueto-Felgueroso, I. Colominas, X. Nogueira, F. Navarrina, M. Casteleiro, Finite-volume solvers and moving least-squares approximations for the compressible Navier-Stokes equations on unstructured grids, Comput. Methods Appl. Mech. Eng. 196 (2007) 4712–4736.
[37] V.V. Rusanov, The calculation of the interaction of non-stationary shock waves and obstacles, USSR Comput. Math. Math. Phys. 1 (2) (1962) 304–320.
[38] L. Ramírez, X. Nogueira, J.C. Chassaing, S. Khelladi, I. Colominas, A new higher-order finite volume method based on Moving Least Squares for the resolution of the incompressible Navier-Stokes equations on unstructured grids, Comput. Methods Appl. Mech. Eng. 278 (2014) 883–901.
[39] S. Gottlieb, C.W. Shu, Total variation diminishing Runge-Kutta schemes, Math. Comput. 67 (221) (1998) 73–85.
[40] L. Ramírez, C. Foulquie, X. Nogueira, S. Khelladi, J.C. Chassaing, I. Colominas, New high-resolution-preserving sliding mesh techniques for higher-order finite volume schemes, Comput. Fluids 118 (2015) 114–130.
[41] K.R. Lee, J.H. Park, K.H. Kim, High-order interpolation method for overset grid based on finite volume method, AIAA J. 49 (2011) 1387–1398.
[42] S.E. Sherer, J.N. Scott, High-order compact finite-difference methods on general overset grids, J. Comput. Phys. 210 (2005) 459–496.
[43] R. Antona, R. Vacondio, D. Avesani, M. Righetti, M. Renzi, Towards a high order convergent ALE-SPH scheme with efficient WENO spatial reconstruction, Water 13 (2021) 2432.
[44] G.I. Taylor, A.E. Green, Mechanism of the production of small eddies from large ones, Proc. R. Soc. Lond. Ser. A, Math. Phys. Sci. 158 (895) (1937) 499–521.
[45] X.Y. Hu, N. Adams, An incompressible multi-phase SPH method, J. Comput. Phys. 227 (1) (2007) 264–278.
[46] A. Krimi, L. Ramírez, S. Khelladi, F. Navarrina, M. Deligant, X. Nogueira, Improved δ-SPH scheme with automatic and adaptive numerical dissipation, Water 12 (10) (2020) 2858.
[47] P.N. Sun, A. Colagrossi, S. Marrone, M. Antuono, A.M. Zhang, A consistent approach to particle shifting in the δ-plus-SPH model, Comput. Methods Appl. Mech. Eng. 348 (2019) 912–934.
[48] J.C. Chassaing, S. Khelladi, X. Nogueira, Accuracy assessment of a high-order moving least squares finite volume method for compressible flows, Comput. Fluids 71 (2013) 41–53.
[49] X.D. Niu, Y.T. Chew, C. Shu, Simulation of flows around an impulsively started circular cylinder by Taylor series expansion- and least squares-based lattice Boltzmann method, J. Comput. Phys. 188 (1) (2003) 176–193.
[50] X. He, G. Doolen, Lattice Boltzmann method on curvilinear coordinates system: flow around a circular cylinder, J. Comput. Phys. 134 (2) (1997) 306–315.
[51] S. Marrone, A. Colagrossi, M. Antuono, G. Colicchio, G. Graziani, An accurate SPH modeling of viscous flows around bodies at low and moderate Reynolds numbers, J. Comput. Phys. 245 (2013) 456–475.
[52] C. Liu, X. Zheng, C.H. Sung, Preconditioned multigrid methods for unsteady incompressible flows, J. Comput. Phys. 139 (1) (1998) 35–57.
[53] B.N. Rajani, A. Kandasamy, S. Majumdar, Numerical simulation of laminar flow past a circular cylinder, Appl. Math. Model. 33 (3) (2009) 1228–1247.
[54] Y.T. Ng, C. Min, F. Gibou, An efficient fluid-solid coupling algorithm for single-phase flows, J. Comput. Phys. 228 (23) (2009) 8807–8829.
[55] E. Constant, J. Favier, M. Meldi, P. Meliga, E. Serre, An immersed boundary method in OpenFOAM: verification and validation, Comput. Fluids 157 (2017) 55–72.
[56] M. Vanella, E. Balaras, A moving-least-squares reconstruction for embedded-boundary formulations, J. Comput. Phys. 228 (18) (2009) 6617–6628.
[57] E. Guilmineau, P. Queutey, A numerical simulation of vortex shedding from an oscillating circular cylinder, J. Fluids Struct. 16 (6) (2002) 773–794.
[58] X.Y. Lu, C. Dalton, Calculation of the timing of vortex formation from an oscillating cylinder, J. Fluids Struct. 10 (5) (1996) 527–541.
[59] W.T. Liu, P.N. Sun, F.R. Ming, A.M. Zhang, Application of particle splitting method for both hydrostatic and hydrodynamic cases in SPH, Acta Mech. Sin. 34 (4) (2018) 601–613.
[60] C. Liu, C. Hu, An efficient immersed boundary treatment for complex moving object, J. Comput. Phys. 274 (2014) 654–680.
[61] X. Sun, J.Z. Zhang, X.L. Ren, Characteristic-based split (CBS) finite element method for incompressible viscous flow with moving boundaries, Eng. Appl. Comput. Fluid Mech. 6 (3) (2012) 461–474.
[62] S. Lee, S.K. Lele, P. Moin, Eddy shocklets in decaying compressible turbulence, Phys. Fluids A, Fluid Dyn. 3 (4) (1991) 657–664.

[63] D. Rizzetta, M. Visbal, G. Blaisdell, Application of a high-order compact difference scheme to large-eddy and direct numerical simulation, in: 30th Fluid Dynamics Conference, AIAA, 1999.
[64] E.T. Spyropoulos, G.A. Blaisdell, Evaluation of the dynamic model for simulations of compressible decaying isotropic turbulence, AIAA J. 34 (5) (1996) 990–998.
[65] S. Hickel, C.P. Egerer, J. Larsson, Subgrid-scale modeling for implicit large eddy simulation of compressible flows and shock-turbulence interaction, Phys. Fluids 26 (10) (2014) 106101.
[66] D.V. Kotov, H.C. Yee, A.A. Wray, B. Sjögreen, A.G. Kritsuk, Numerical dissipation control in high order shock-capturing schemes for LES of low speed flows, J. Comput. Phys. 307 (2016) 189–202.
[67] S. Sarkar, G. Erlebacher, M.Y. Hussaini, H.O. Kreiss, The analysis and modelling of dilatational terms in compressible turbulence, J. Fluid Mech. 227 (1991) 473–493.
[68] E. Garnier, N. Adams, P. Sagaut, Large Eddy Simulation for Compressible Flow, Scientific Computation Springer, 2009.
[69] M.R. Visbal, D.P. Rizzetta, Large-eddy simulation on curvilinear grids using compact differencing and filtering schemes, J. Fluids Eng. 124 (4) (2004) 836–847.
[70] A.E. Honein, P. Moin, Higher entropy conservation and numerical stability of compressible turbulence simulations, J. Comput. Phys. 201 (2) (2004) 531–545.
[71] M. Hussaini, On large-eddy simulation of compressible flows, in: 29th AIAA Fluid Dynamics Conference, vol. 12, 1998.
[72] C.W. Shu, W.S. Don, D. Gottlieb, O. Schilling, L. Jameson, Numerical convergence study of nearly incompressible, inviscid Taylor-Green vortex flow, J. Sci. Comput. 24 (2005) 1–27.
[73] J. Fernández-Fidalgo, L. Ramírez, P. Tsoutsanis, I. Colominas, X. Nogueira, A reduced-dissipation WENO scheme with automatic dissipation adjustment, J. Comput. Phys. 425 (2021) 109749.
[74] M.E. Brachet, D.I. Meiron, S.A. Orszag, B.G. Nickel, R.H. Morf, U. Frisch, Small-scale structure of the Taylor-Green vortex, J. Fluid Mech. 130 (1983) 411–452.
[75] N. Fehn, M. Kronbichler, P. Munch, W. Wall, Numerical evidence of anomalous energy dissipation in incompressible Euler flows: towards grid-converged results for the inviscid Taylor-Green problem, arXiv:2007.01656, 2020.
[76] D.J. Garmann, M.R. Visbal, AFRL contributions to the third international workshop on high-order CFD methods, in: Third International Workshop on High-Order CFD Methods, 2015.